

Three-Dimensional Optical–Electrical Simulation of $\text{Cs}_2\text{AgBiBr}_6$ Double Perovskite Solar Cells

Md Shanian Moed, Adnan Amin Siddiquee, and Md Tashfiq Bin Kashem*

Department of Electrical and Electronic Engineering, Ahsanullah University of Science and Technology, Dhaka – 1208, Bangladesh

* Corresponding author: E-mail address: tashfiq.eee@aust.edu

Abstract

Despite significant advances in lead-free perovskite photovoltaics, achieving a balance among environmental safety, long-term stability, and high optoelectronic performance remains challenging. The inorganic double perovskite $\text{Cs}_2\text{AgBiBr}_6$ has emerged as a promising candidate owing to its robust three-dimensional crystal structure, suitable visible-range bandgap, and excellent thermal and moisture stability. However, best power conversion efficiencies (PCEs) for $\text{Cs}_2\text{AgBiBr}_6$ solar cells reported so far – 6.37% experimentally and 27.78% in numerical studies – remain below the theoretical performance potential predicted for optimized single-junction architectures, largely due to suboptimal charge transport layers, and interface-related recombination losses. Here, we address this gap using a three-dimensional (3D) finite-element method (FEM) implemented in COMSOL Multiphysics, which couples full-wave optical simulations with semiconductor drift–diffusion transport. To our knowledge, this work represents the first comprehensive 3D FEM-based study of a double halide perovskite solar cell, enabling quantitative resolution of architecture- and interface-driven losses. Screening of 25 electron transport layer (ETL)–hole transport layer (HTL) combinations identifies CeO_2 and P3HT as the optimal ETL and HTL respectively. Device performance is further analyzed through systematic variation of layer thicknesses, doping concentrations, defect densities, and intrinsic recombination parameters within the FTO/ CeO_2 / $\text{Cs}_2\text{AgBiBr}_6$ /P3HT/Au architecture. Under optimized parameters, the simulated device achieves a PCE of 31.76%, representing the theoretical upper bound predicted by the model. Overall, this work demonstrates 3D physics-based device engineering as a decisive pathway for overcoming efficiency bottlenecks in lead-free double perovskite photovoltaics, while providing a modeling framework applicable to perovskite solar cells beyond $\text{Cs}_2\text{AgBiBr}_6$.

Keywords: Lead-free double perovskite solar cell; $\text{Cs}_2\text{AgBiBr}_6$; 3D finite-element method; COMSOL Multiphysics

1. Introduction

The urgent need to mitigate climate change and reduce dependence on fossil fuel–based power generation has accelerated the global transition toward clean and renewable energy technologies [1], [2]. Among the available renewable resources, solar energy is the most abundant and universally accessible, making photovoltaic (PV) conversion a central pillar of future sustainable energy systems [3]. While crystalline silicon solar cells continue to dominate the commercial market due to their technological maturity, their energy-intensive manufacturing and high processing temperatures motivate continued exploration of alternative absorber materials capable of delivering high efficiency through scalable, low-temperature fabrication routes [4][5]. Third-generation photovoltaic technologies—including dye-sensitized, organic, quantum dot, and perovskite solar cells—have therefore attracted extensive research interest [6]. In particular, lead (Pb)-based hybrid organic–inorganic halide perovskites have achieved a remarkable rise in power conversion efficiency (PCE), from 3.8% in 2009 [7] to 26.95% in 2025 [8], approaching crystalline silicon benchmarks. These materials typically adopt the ABX_3 perovskite structure (Fig. 1a), where A denotes a larger organic or inorganic cation (CH_3NH_3^+ , $\text{CH}(\text{NH}_2)_2^+$, Cs^+ , K^+ , Na^+ etc.), B corresponds to a divalent metal cation—most commonly Pb^{2+} —and X represents a halide anion (I^- , Br^- , or Cl^-). This crystal model enables compositional tunability while supporting the outstanding optoelectronic properties of perovskite absorbers, including strong optical absorption, long carrier diffusion lengths, low exciton binding energies, and balanced charge transport [9]. However, despite these exceptional properties, large-scale deployment remains constrained by Pb toxicity and long-term instability associated with

volatile organic cations [10]–[12]. These concerns have driven the search for environmentally benign, structurally stable, lead-free alternatives.

Early substitution strategies replacing Pb^{2+} with Sn^{2+} or Ge^{2+} were motivated by chemical similarity but suffer from rapid oxidation and severe defect formation, leading to instability and performance degradation [13]–[16]. Alternatively, Pb^{2+} substitution using heterovalent cation combinations has led to the emergence of several families of lead-free halide perovskite derivatives formed to satisfy charge neutrality. These materials span a range of structural motifs, including $\text{A}_3\text{B}_2^{3+}\text{X}_9$, $\text{A}_2\text{B}^{4+}\text{X}_6$ and related low-symmetry or vacancy-ordered variants, where A-site cations are typically monovalent (e.g., Cs^+ , Rb^+ , K^+ , or organic cations such as $\text{CH}_3\text{NH}_3^+/\text{CH}(\text{NH}_2)_2^+$) and B-site cations include trivalent or monovalent metals (e.g., Bi^{3+} , Sb^{3+} , In^{3+} , Ag^+ , Cu^+ , Na^+) [17], [18]. While these compositions incorporate environmentally benign cations, their crystal structures are typically zero- to two-dimensional in nature. This reduced dimensionality inherently limits carrier mobility and enhances recombination, resulting in suboptimal photovoltaic performance [19]–[21].

Three-dimensional halide double perovskites (HDPs) with general formula $\text{A}_2\text{B}'\text{B}''\text{X}_6$ offer a promising pathway to overcome both toxicity and dimensionality limitations [10]. In these materials, Pb^{2+} is replaced by a monovalent (B') and a trivalent (B'') cation, while preserving the three-dimensional perovskite framework (Fig. 1b). This design strategy offers substantial compositional flexibility through diverse choices of A, B' , and B'' -site ions, allowing systematic tuning of band structure, carrier transport, and thermodynamic stability [22]–[25].

Among the reported HDPs, $\text{Cs}_2\text{AgBiBr}_6$ —crystallizing in the cubic elpasolite-type double perovskite structure (space group $\text{Fm}\bar{3}\text{m}$)—has attracted particular attention as a benchmark inorganic lead-free perovskite absorber [11], [26]. The cooperative incorporation of Ag^+ and Bi^{3+} at the B' and B'' -sites enhances lattice stability, resulting in a high decomposition energy and exceptional resistance to thermal and moisture-induced degradation [27]. In addition to its robust structural stability, $\text{Cs}_2\text{AgBiBr}_6$ exhibits a suitable visible-range bandgap, long radiative and nonradiative carrier lifetimes, relatively low carrier effective masses, and notable defect tolerance—properties that are essential for efficient photovoltaic operation [10], [22], [28]. Importantly, several of these optoelectronic

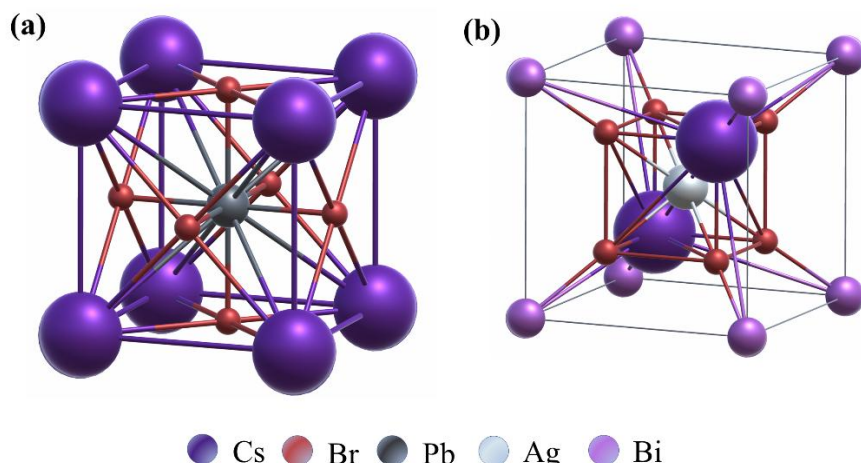


Fig. 1. Schematic crystal structures showing the atomic site occupation of (a) perovskite and (b) double perovskite materials.

characteristics approach those of archetypal Pb-based perovskites, while offering the decisive advantages of low toxicity and long-term environmental compatibility [29]–[31].

Since its initial incorporation into photovoltaic devices by Greul *et al.* [32] using a planar FTO/TiO₂/Cs₂AgBiBr₆/Spiro-OMeTAD/Au architecture, which delivered a PCE of 2.43% and established the experimental feasibility of this absorber, Cs₂AgBiBr₆ has been explored extensively across diverse device architectures, contact layer combinations, and deposition routes, including both solution-processed and vapor-deposited films [33], [34]. Continuous experimental progress has led to the current record efficiency of 6.37%, achieved by Zhang *et al.* via optimized planar architectures (ITO/SnO₂/Cs₂AgBiBr₆/Spiro-OMeTAD/Au), demonstrating excellent operational stability (1440h at 85°C) as well [28]; however, the performance remains modest relative to Pb-based counterparts. In parallel, numerical studies suggest that significantly higher efficiencies may be achievable through appropriate selection of charge transport layers and careful optimization of material and interfacial parameters [35]–[38]. For instance, Danladi *et al.* reported a PCE of 25.56% for the FTO/ZnO/Cs₂AgBiBr₆/CFTS/Au structure [36]. Hakami *et al.* proposed an all-inorganic device architecture based on FTO/TiO₂/Cs₂AgBiBr₆/NiO/Au, achieving a simulated PCE of 26.71% [37]. Similarly, Srivastava *et al.* identified an optimized planar FTO/AZO/Cs₂AgBiBr₆/ZnTe configuration, predicting a PCE of 26.89% [35]. More recently, Raj *et al.* reported an optimized efficiency of 27.78% for the FTO/TiO₂/Cs₂AgBiBr₆/Cu₂O/Au structure [38]. Collectively, these insights motivate a systematic device-level optimization strategy in which suitable electron transport layer (ETL)–hole transport layer (HTL) combinations are first identified, followed by targeted tuning of layer

thicknesses, doping concentrations, and bulk and interfacial defect densities, with the aim of identifying realistic pathways toward performance enhancement in Cs₂AgBiBr₆-based solar cells. Despite the advances, most prior modeling efforts rely on one-dimensional drift–diffusion solvers that assume simplified generation profiles and neglect spatial optical redistribution and multidimensional interfacial effects. Therefore, realistic modeling of optical field distribution and its coupling to carrier transport is essential for identifying true performance limits and dominant loss mechanisms.

In this context, physics-based finite-element modeling offers a powerful framework for resolving coupled optical and electrical phenomena in heterogeneous device stacks. COMSOL Multiphysics enables self-consistent solutions of Maxwell’s equations and semiconductor transport equations within multidimensional geometries, allowing spatially resolved analysis of photogeneration, band bending, quasi-Fermi level splitting, and recombination processes [39]–[42]. However, such a coupled three-dimensional (3D) treatment remains largely unexplored for Cs₂AgBiBr₆-based solar cells.

Motivated by this gap, the present work develops a comprehensive 3D finite-element opto-electrical framework to investigate Cs₂AgBiBr₆ solar cells across multiple charge transport layer combinations. Twenty-five ETL–HTL pairings are systematically screened to identify optimal contact materials. Building upon the most favorable configuration, layer thicknesses, doping concentrations, bulk and interfacial defect densities, intrinsic recombination coefficients, temperature, and illumination intensity are rigorously examined. By explicitly calculating optical generation profiles and coupling them to drift–diffusion transport, this integrated framework establishes physically grounded performance bounds, identifies critical design tolerance windows, and explains the fundamental loss mechanisms governing Cs₂AgBiBr₆ photovoltaics, thereby providing quantitative guidance toward experimentally realizable, high-efficiency lead-free double perovskite solar cells.

2. Simulation Framework

2.1 Device Structure and Material Parameters

All simulations were carried out using a three-dimensional finite-element method in COMSOL Multiphysics framework. The investigated device architecture adopts a layered heterojunction configuration of FTO/ETL/Cs₂AgBiBr₆/HTL/Au (Fig. 2a). A schematic of the equilibrium energy-band alignment of the complete device stack is shown in Fig. 2b.

Fluorine-doped tin oxide (FTO) is employed as the transparent front electrode due to its high optical transmittance in the visible region and excellent chemical and thermal stability, making it a well-established and reliable choice for perovskite and inorganic thin-film photovoltaic devices [43].

An ETL is introduced between FTO and the absorber to enable selective extraction of photogenerated electrons while suppressing hole transport toward the front contact. To assess the influence of transport-layer properties, five representative ETL materials – AZO (aluminum-doped zinc oxide), CeO₂ (cerium (IV) oxide), WS₂ (tungsten disulphide), C₆₀ (buckminsterfullerene) and PCBM ([6,6]-phenyl-C₆₁-butyric acid methyl ester) – were examined. These materials span a broad range of electronic characteristics, including wide-bandgap metal oxides, layered inorganic semiconductors, and organic fullerene derivatives [44][45]. Such diversity allows a comprehensive evaluation of band alignment, carrier mobility, optical transparency, and interfacial recombination behavior within the device.

Cs₂AgBiBr₆ is employed as the absorber layer, where photon absorption and electron–hole pair generation occur under illumination. In the simulated architecture, carrier transport within the absorber

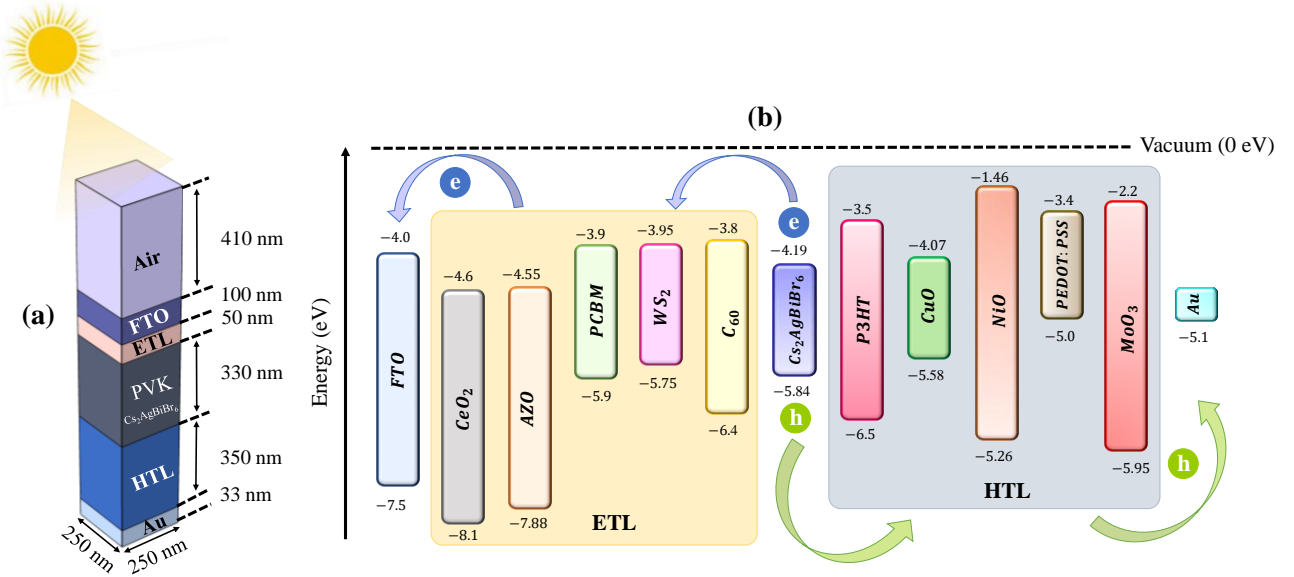


Fig. 2. (a) Schematic illustration of the Cs₂AgBiBr₆ perovskite (PVK) absorber-based solar cell architecture, with the individual layer thicknesses; detailed material parameters are listed in Tables 1-3. (b) Energy band alignment diagram showing the conduction band minima (CBM) and valence band maxima (VBM) of the constituent layers; for each material, the upper and lower numerical values denote the CBM and VBM energy levels, respectively. Five electron transport layers (ETLs)—CeO₂, AZO, PCBM, WS₂, and C₆₀—and five hole transport layers (HTLs)—P3HT, CuO, NiO, PEDOT:PSS, and MoO₃—were investigated. The conduction and valence band offsets (CBO, VBO) at the absorber/ETL and absorber/HTL interfaces are summarized in Tables 4 and 5. The symbols “e” and “h” in panel (b) represent electrons and holes. Under illumination, photogenerated electron–hole pairs are created within the Cs₂AgBiBr₆ absorber; electrons are transported toward the FTO front contact through the ETL, while holes are collected at the Au back contact via the HTL.

is governed by bulk material properties, defect-assisted recombination, and interfacial charge transfer at the ETL and HTL interfaces.

On the rear side of the absorber, a HTL is incorporated to facilitate efficient extraction of photogenerated holes while blocking electron transport toward the back contact. Five HTL materials – P3HT (poly(3-hexylthiophene)), PEDOT:PSS (Poly(3,4-ethylenedioxythiophene) polystyrene sulfonate), CuO (copper (II) oxide), NiO (nickel (II) oxide) and MoO₃ (molybdenum trioxide) – were considered, representing polymeric, oxide, and transition-metal-oxides, with distinct valence-band alignments and hole transport characteristics. These materials have been extensively reported as effective HTLs in perovskite and thin-film solar cells and provide a suitable basis for systematic transport-layer engineering [46], [47].

Gold (Au), with a high work function of approximately 5.1 eV, is selected as the back contact to ensure favorable energetic alignment with the HTL and efficient hole collection while minimizing contact resistance. The top and bottom electrodes of the device were modeled as Ohmic contacts by applying Dirichlet boundary conditions for the electrostatic potential. In COMSOL, these conditions directly fix the potential at the contact nodes, ensuring that the applied voltage is correctly enforced during the solution of the semiconductor equations. The applied voltage bias was introduced at the back contact, while the front contact was grounded. All other external boundaries were treated as electrically insulating to prevent unintended current flow. An air domain was included above the FTO front electrode to represent the surrounding optical medium and to correctly impose the incident

Table 1. Input parameters of FTO, Cs₂AgBiBr₆, and HTL materials: band gap (E_g), electron affinity (χ), relative dielectric permittivity (ϵ_r), effective density of states in the conduction band (N_c), effective density of states in the valence band (N_v), electron mobility (μ_n), hole mobility (μ_p), acceptor density (N_A), donor density (N_D), and defect density (N_t)

Parameters	FTO	Cs ₂ AgBiBr ₆	P3HT	CuO	NiO	PEDOT:PSS	MoO ₃
Thickness (nm)	100	300	350	350	350	350	350
E_g (eV)	3.5	1.654	1.7	1.51	3.8	1.6	3.75
χ (eV)	4	4.19	3.5	4.07	1.46	3.4	2.2
ϵ_r	9	5.8	3	18.1	10.7	3	4.45
N_c (1/cm ³)	2.2×10^{18}	1×10^{16}	2×10^{21}	2.2×10^{19}	2.8×10^{19}	2.2×10^{18}	1×10^{19}
N_v (1/cm ³)	1.8×10^{19}	1×10^{16}	2×10^{21}	5.5×10^{20}	10^{19}	1.8×10^{19}	1×10^{19}
μ_n (cm ² /Vs)	2×10^1	1.81	1.8×10^{-3}	100	12	4.5×10^{-2}	1.1×10^3
μ_p (cm ² /Vs)	1×10^1	0.49	1.86×10^{-2}	0.1	2.8	4.5×10^{-2}	1.1×10^3
N_A (1/cm ³)	1	3×10^{15}	10^{18}	1×10^{18}	1×10^{18}	1×10^{18}	2×10^{18}
N_D (1/cm ³)	1×10^{19}	0	0	0	0	0	0
N_t (1/cm ³)	10^{14}	10^{14}	10^{14}	10^{15}	10^{15}	10^{15}	10^{15}
Reference	[37]	[48]	[49]	[50]	[51]	[52]	[53]

Table 2. Input parameters of ETL materials

Parameters	AZO	CeO ₂	PCBM	WS ₂	C ₆₀
Thickness (nm)	30	30	30	30	30
E_g (eV)	3.33	3.5	2	1.8	1.7
χ (eV)	4.55	4.6	3.9	3.95	3.9
ϵ_r	8.12	9	3.9	13.6	4.2
N_C (1/cm ³)	4.1×10^{18}	1×10^{20}	2×10^{21}	1×10^{18}	8×10^{19}
N_V (1/cm ³)	8.2×10^{19}	2×10^{21}	2×10^{21}	2.4×10^{19}	8×10^{19}
μ_n (cm ² /Vs)	20	100	0.2	100	8×10^{-2}
μ_p (cm ² /Vs)	10	25	0.2	100	8×10^{-3}
N_A (1/cm ³)	0	0	0	0	0
N_D (1/cm ³)	1×10^{19}	2×10^{21}	2.93×10^{17}	10^{18}	1×10^{17}
N_t (1/cm ³)	10^{15}	10^{15}	10^{15}	10^{15}	10^{15}
Reference	[54]	[50]	[55]	[56]	[55]

Table 3. Input parameters for interface and bulk defects

Parameters	ETL/Cs ₂ AgBiBr ₆ interface	Cs ₂ AgBiBr ₆ /HTL interface	Bulk Cs ₂ AgBiBr ₆
Defect type	Neutral	Neutral	Neutral
Electron capture cross section (cm ²)	10^{-18}	10^{-18}	10^{-15}
Hole capture cross section (cm ²)	10^{-18}	10^{-18}	10^{-15}
Energetic distribution	Single	Single	Single
Thermal velocity (cm/s)	1×10^7	1×10^7	1×10^7
Impurity energy level	Midgap	Midgap	Midgap
Total density (cm ⁻²)	10^{10} (Variable)	10^{10} (Variable)	10^{14} cm ⁻³ (Variable)

Table 4. CBO between Cs₂AgBiBr₆ and ETL materials: CBO = $\chi_{\text{absorber}} - \chi_{\text{ETL}}$

ETL	AZO	CeO ₂	PCBM	WS ₂	C ₆₀
CBO	0.35	0.4	-0.3	-0.25	-0.3

Table 5. VBO between Cs₂AgBiBr₆ and HTL materials: VBO = $(\chi_{\text{HTL}} + E_g, \text{HTL}) - (\chi_{\text{absorber}} + E_g, \text{absorber})$

HTL	P3HT	CuO	NiO	PEDOT-PSS	MoO ₃
VBO	0.04	-0.34	-0.02	0.24	-0.71

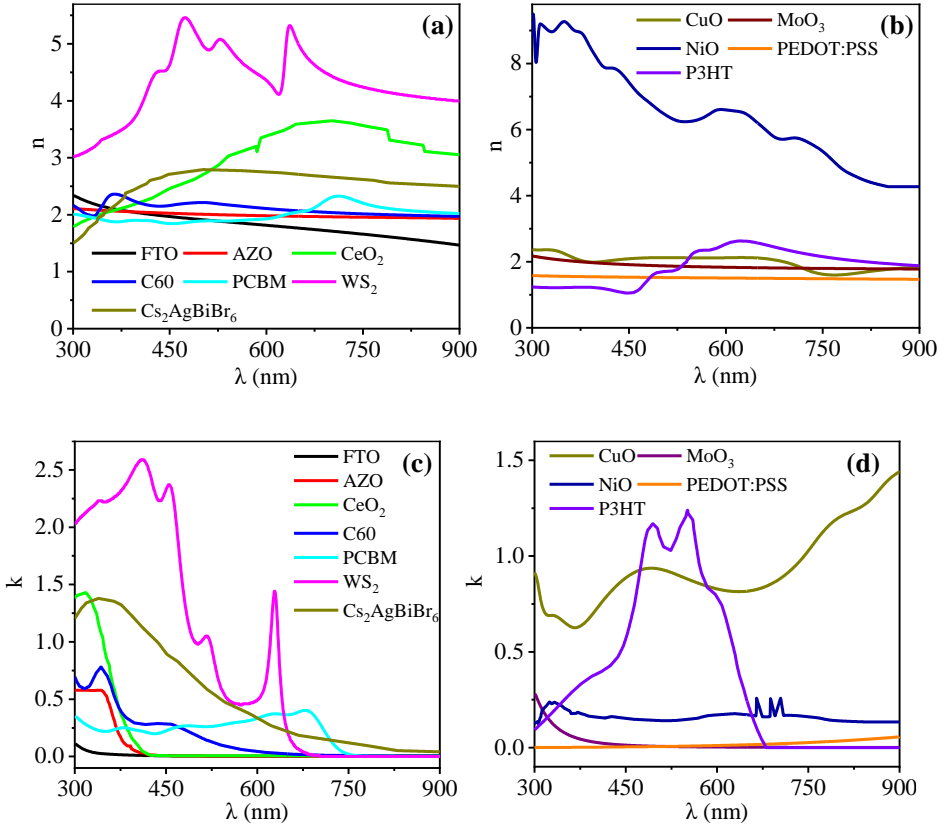


Fig. 3. (a,b) Refractive index (n) and (c,d) extinction coefficient (k) spectra of the FTO, absorber, ETL and HTL materials used in the simulations, extracted from Refs. [48], [57]–[67].

electromagnetic boundary conditions. All the material parameters – including bandgaps, electron affinities, dielectric constants, and carrier mobilities – were adopted from previously reported literature.

Unless otherwise stated, all simulations were performed under standard AM1.5G illumination with an incident power density of 1000 W m^{-2} at an operating temperature of 300 K. The complete set of material, and interface parameters employed in the simulations is summarized in Tables 1-5 and Fig. 3.

2.2 Mesh Generation

A user-controlled, structured mesh was employed for the six-layer device architecture. Each domain was discretized individually with minimum and maximum element sizes of 1.91 nm and 22 nm, respectively. The maximum element growth rate was set to 1.08 with a curvature factor of 0.3 and narrow region resolution of 0.95 to ensure accurate resolution of sharp interfacial gradients. A hybrid meshing scheme combining free triangular elements (surface) and swept quadrilateral elements (volume) was implemented. The top and bottom faces were meshed using free triangular elements, while remaining faces were discretized using a swept quadrilateral sequence. Thickness-dependent element distributions were applied across domains using a combination of linear and exponential growth profiles. For example, the 50 nm ETL layer was discretized into 80 elements with symmetric linear grading, whereas the perovskite absorber was initially resolved with 50 elements using exponential grading (growth ratio = 5), ensuring refined meshing near the ETL/perovskite heterointerface. Tessellation was set to automatic. Adaptive mesh refinement was enabled to dynamically resolve regions exhibiting large gradients in electrostatic potential, carrier concentration,

and recombination rate. Depending on the device configuration, the total number of degrees of freedom (DOFs) solved ranged from approximately 3.24×10^4 for the initial structure to 2.58×10^5 for the optimized device. Mesh independence was confirmed by progressively increasing mesh density until the current–voltage characteristics exhibited negligible variation. Mesh quality was evaluated using skewness and growth rate metrics; the resulting distributions satisfied standard quality criteria, confirming numerical stability and solution convergence.

2.3 Theoretical Formulation

The simulations were performed by coupling the Electromagnetic Waves, Frequency Domain (EWFD) interface with the Semiconductor interface within COMSOL Multiphysics. The coupled approach enables the calculation of optical absorption and photogeneration using full-wave electromagnetic analysis, followed by charge carrier transport using a drift–diffusion formalism.

2.3.1 Optical Simulation Using EWFD Interface

The optical response of the device under illumination was computed using the EWFD interface, which solves Maxwell's equations in three dimensions in the frequency domain to obtain the wavelength-dependent electric field distribution, $\mathbf{E}(\lambda)$ [68]:

$$\nabla \times \mu_r^{-1}(\nabla \times \mathbf{E}) - k_0^2 \epsilon_r \mathbf{E} = 0 \quad (1)$$

where \mathbf{E} denotes the electric field vector, ϵ_r and μ_r are the relative permittivity and permeability of the materials, respectively, and k_0 is the free-space wave number. ϵ_r and k_0 are expressed as [69],

$$\epsilon_r = \epsilon' + \epsilon'' = [n(\lambda) - jk(\lambda)]^2 \quad (2)$$

$$k_0 = \frac{\omega}{c_0} \quad (3)$$

where ϵ' and ϵ'' are the real and imaginary parts of ϵ_r , respectively; n and k are refractive index and extinction coefficient, respectively; ω is the angular frequency of the incident radiation, and c_0 is the speed of light in vacuum.

A normally incident plane wave corresponding to the AM1.5G solar spectrum was applied at the FTO side to represent solar irradiation. The wavelength-dependent n and k of each layer were incorporated to account for optical dispersion and absorption. The local volumetric absorbed power density at each wavelength was calculated as:

$$Q_{abs}(x, y, z, \lambda) = \frac{1}{2} \omega(\lambda) \epsilon_0 \epsilon''(\lambda) |\mathbf{E}(x, y, z, \lambda)|^2 \quad (4)$$

Here, ϵ_0 is the vacuum permittivity, and $|\mathbf{E}|$ represents the magnitude of the electric field. The photogeneration rate at each wavelength was then computed as [69],

$$G_{opt}(x, y, z, \lambda) = \frac{Q_{abs}(x, y, z, \lambda)}{h v(\lambda)} \quad (5)$$

Here h is Planck's constant and v is the photon frequency. To account for the full spectral range of illumination, the wavelength-dependent generation rate was integrated over the relevant wavelength interval for each layer:

$$G_{tot}(x, y, z) = \int_{\lambda_{min}}^{\lambda_{max}} G_{opt}(\lambda) d\lambda \quad (6)$$

The spectrally integrated generation profile was then volume-averaged and applied to the corresponding layers in Semiconductor physics module, where it served as the photogeneration term in the carrier continuity equations for drift-diffusion simulations.

2.3.2 Charge Transport Modeling in Semiconductor Interface

Electrical modeling was performed using the Semiconductor interface, which solves Poisson's equation coupled with the electron and hole continuity equations within the drift-diffusion approximation.

The electrostatic potential Φ is governed by Poisson's equation:

$$\nabla \cdot (\epsilon \nabla \Phi) = -q(p - n + N_D^+ - N_A^-) \quad (7)$$

where ϵ is the relative permittivity, q is the elementary charge, n and p are the electron and hole concentrations, and N_D^+ and N_A^- represent ionized donor and acceptor densities.

The continuity equations for electrons and holes are given by:

$$\nabla \cdot \mathbf{J}_n = q(G_n - R_n) \quad (8)$$

$$\nabla \cdot \mathbf{J}_p = q(G_p - R_p) \quad (9)$$

where G is the total carrier generation rate, including photogeneration, and R is the recombination rate. The subscripts n and p correspond to electron and hole, respectively.

The electron and hole current densities are expressed as:

$$\mathbf{J}_n = q\mu_n n \nabla \Phi + qD_n \nabla n \quad (10)$$

$$\mathbf{J}_p = q\mu_p p \nabla \Phi - qD_p \nabla p \quad (11)$$

where μ is the carrier mobility, and D is the diffusion coefficient, related to the mobilities through the Einstein relation:

$$D_{n,p} = \mu_{n,p} \frac{kT}{q} \quad (12)$$

Where k is the Boltzmann constant and T is temperature. Carrier recombination within the device was modeled using three primary mechanisms: Shockley-Read-Hall (SRH), radiative (direct), and Auger recombination. SRH recombination accounts for defect-mediated, nonradiative recombination:

$$R_{SRH} = \frac{np - n_i^2}{\tau_p(n+n_i) + \tau_n(p+n_i)} \quad (13)$$

where n_i is the intrinsic carrier concentration, and τ_n and τ_p are the electron and hole lifetimes, respectively. Radiative (direct) recombination describes band-to-band recombination:

$$R_{Rad} = C_{Radiative} (np - n_i^2) \quad (14)$$

where $C_{Radiative}$ is the radiative recombination coefficient. Auger recombination models three-particle interactions, significant at high carrier densities:

$$R_{Auger} = C_{n,Auger} n(np - n_i^2) + C_{p,Auger} p(np - n_i^2) \quad (15)$$

where $C_{n,Auger}$ and $C_{p,Auger}$ are the Auger coefficients for electrons and holes, respectively.

2.3.3 Performance Parameters

The coupled optical–electrical problem was solved using a stationary solver. From the converged solutions, current density–voltage (J–V) characteristics under illumination were extracted, and key photovoltaic parameters—including short-circuit current density (J_{SC}), open-circuit voltage (V_{OC}), fill factor (FF), and PCE—were calculated.

$$V_{OC} = \frac{kT}{q} \ln \left(\frac{J_{SC}}{J_0} + 1 \right) \quad (16)$$

$$FF = \frac{V_m J_m}{V_{OC} J_{SC}} \quad (17)$$

$$PCE = \frac{V_{OC} J_{SC} FF}{P_{in}} \quad (18)$$

Where J_0 is the reverse saturation current density, V_m and J_m refer to the voltage and current density respectively at the maximum power point, and P_{in} is the input power.

3. Results and Analysis

3.1 Model Validation and Benchmarking

To establish the reliability of the proposed simulation framework, the device model was first validated by reproducing experimentally reported results of a previously published $Cs_2AgBiBr_6$ -based solar cell with the configuration: ITO/SnO₂/Cs₂AgBiBr₆/Spiro-OMeTAD/Au [28]. The simulation parameters, including layer thicknesses and material properties were carefully adopted from the experimental study to ensure a meaningful comparison.

Figure 4 presents a direct comparison between the simulation and experimental results in terms of J–V characteristics under AM1.5G illumination. The simulated curve closely reproduces the experimental response across the entire bias range, capturing both the slope near open-circuit conditions and the curvature around the maximum power point. This agreement indicates that the model accurately describes the dominant carrier transport and recombination processes governing device operation.

In addition to the J–V characteristics, the extracted photovoltaic performance parameters— V_{OC} , J_{SC} , FF, and PCE—are summarized in the Table inside the figure and compared with the values reported

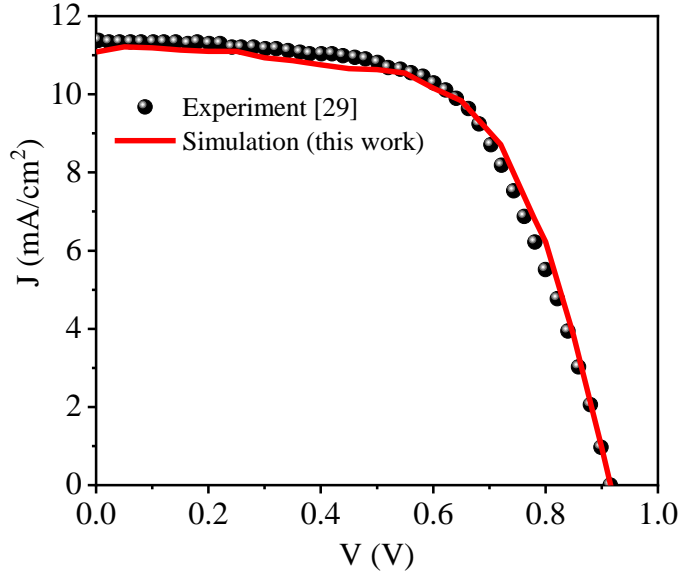


Fig. 4. Benchmarking and validation of the simulation framework presented in this work through comparison with experimentally reported J-V characteristics and associated photovoltaic parameters (V_{oc} , J_{sc} , FF, and PCE) of $Cs_2AgBiBr_6$ -based solar cell [28].

in Ref. [28]. The simulated results show close quantitative agreement with the measured data, with only minor deviations that can reasonably be attributed to experimental uncertainties, material inhomogeneities, and processing-induced variations not explicitly captured in the numerical model.

Overall, the strong agreement between simulation and experiment confirms the validity of the adopted physical models and parameter sets. This validation provides a solid foundation for systematic transport-layer engineering, followed by broader material and device-level parametric investigations aimed at optimizing the performance of the $Cs_2AgBiBr_6$ -absorber-based solar cell architecture.

3.2 Performance Analysis of ETL-HTL Pairings

A comprehensive charge transport-layer (ETL and HTL) study with 25 distinct ETL/HTL combinations was carried out to identify optimal carrier-selective contacts for the $Cs_2AgBiBr_6$ absorber. The selected transport materials satisfy established selection criteria reported in prior literature [70], including suitable band alignment, sufficient carrier mobility, optical transparency, and chemical stability. V_{oc} , J_{sc} , FF, and PCE were extracted for each combination (Fig. 5), a pronounced dependence of device performance on transport-layer pairing is observed, underscoring the critical role of interfacial energetics and carrier selectivity.

Higher V_{oc} exceeding ~ 1.8 V are achieved for AZO/P3HT, AZO/NiO, CeO_2 /PEDOT:PSS, WS_2 /CuO, and WS_2 /MoO₃ configurations (Fig. 5a). These higher voltages can be attributed to favorable interfacial band alignment and effective suppression of interfacial recombination, which enhance quasi-Fermi level splitting within the absorber. In contrast, combinations with suboptimal energy-level matching exhibit lower V_{oc} , highlighting the sensitivity of voltage output to interface energetics.

Highest J_{sc} of 16.45 mA cm^{-2} is obtained for CeO_2 /P3HT combination (Fig. 5b). This enhanced current response reflects the excellent optical transparency of CeO_2 in the visible spectrum, combined with efficient electron extraction and minimal parasitic absorption in the ETL. Simultaneously, the favorable hole mobility and interfacial compatibility of P3HT facilitate efficient charge collection, leading to superior photogenerated current compared with alternative transport-layer pairings.

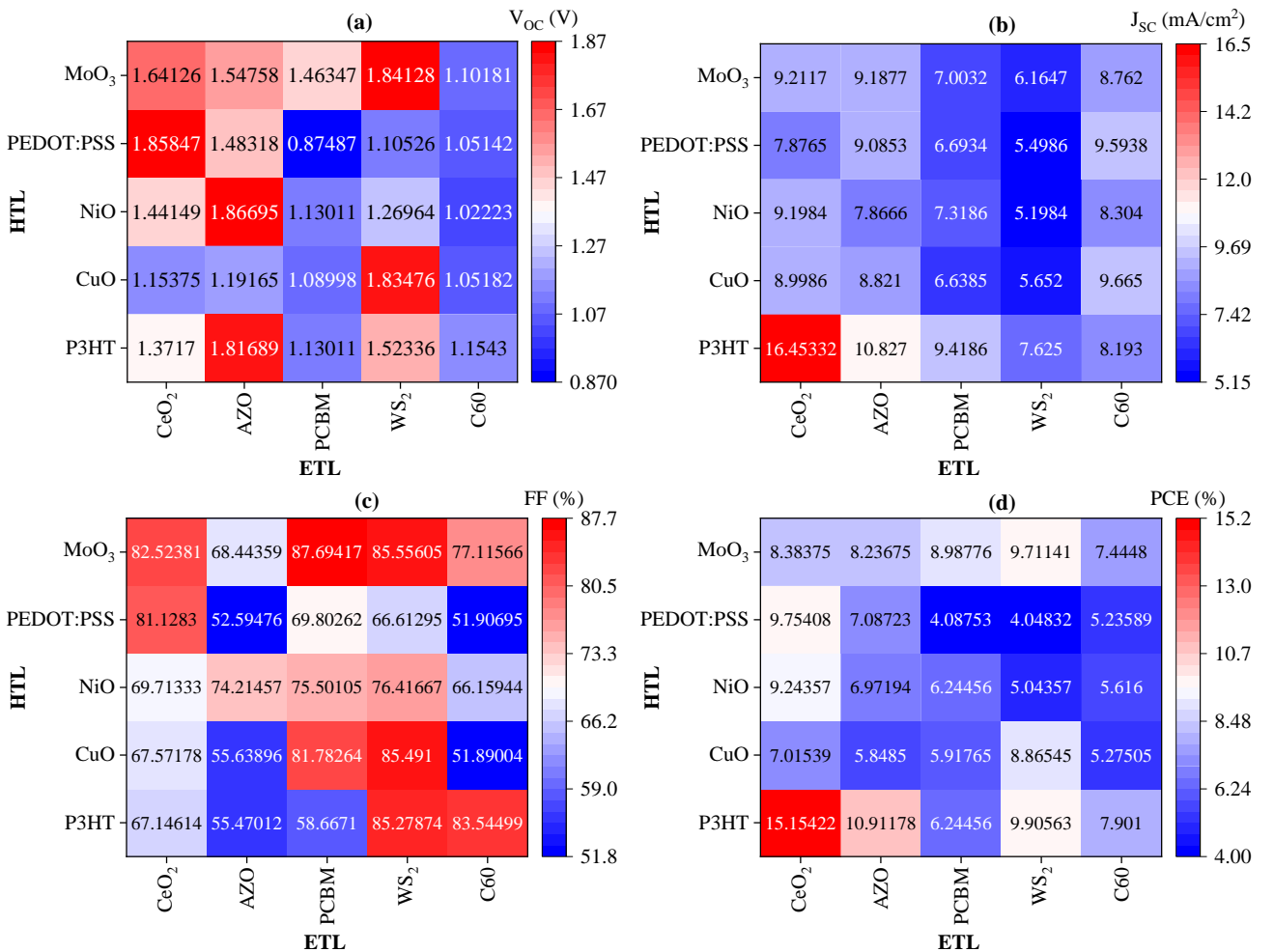


Fig. 5. Comparison of performance parameters for 25 ETL/HTL combinations (5 ETLs \times 5 HTLs), showing (a) V_{OC} , (b) J_{SC} , (c) FF, and (d) PCE. All the simulations were performed using the following layer thicknesses along the z-axis: FTO = 100 nm, ETL = 50 nm, $\text{Cs}_2\text{AgBiBr}_6$ = 330 nm, HTL = 350 nm, and Au = 33 nm.

FF also varies considerably with transport-layer pairing (Fig. 5c). High FF exceeding 85% are achieved for PCBM/MoO₃, WS₂/MoO₃, WS₂/CuO, and WS₂/P3HT configurations. These combinations benefit from reduced series resistance, efficient carrier selectivity, and suppressed recombination losses near the maximum power point, resulting in improved diode rectification and more ideal J–V characteristics.

As a cumulative metric, the PCE reflects the combined trends in V_{OC} , J_{SC} , and FF (Fig. 5d). The highest PCE of 15.15% is obtained for the CeO_2 /P3HT configuration, which simultaneously offers the largest J_{SC} along with competitive V_{OC} and FF values. Other combinations exhibiting high voltage or fill factor alone do not achieve comparable efficiencies due to trade-offs in current generation or resistive losses. These results indicate that balanced optimization of charge extraction, optical transmission, and interfacial recombination is essential for maximizing device efficiency.

Based on this comprehensive comparative assessment, CeO_2 and P3HT emerge as the most promising ETL and HTL, respectively, for $\text{Cs}_2\text{AgBiBr}_6$ absorber-based solar cell. Accordingly, this ETL/HTL pair is selected for subsequent wavelength-resolved optical analysis and detailed material and device-level parametric optimization.

3.3 Optical Response and Carrier Generation Analysis

3.3.1 Wavelength-Dependent Optical Field, Absorbed Power, and Carrier Generation

In this section, the spatial distributions of the optical electric field, local volumetric absorbed power density (Q_{abs}), and carrier generation rate within the full device stack with the optimal charge transport layers (CeO_2 and P3HT), obtained from EWFD module (Fig. 6-8), have been analyzed. 3D visualizations provide a global perspective on light propagation, field localization, and absorption across all layers (Fig. 6-8, a-e). To enable clearer layer-resolved interpretation, two-dimensional (2D) cross-sectional maps were subsequently extracted in the yz -plane at a fixed lateral position ($x = 125$ nm), which intersects all functional layers from the FTO front contact to the Au back electrode (Fig. 6-8, f-j).

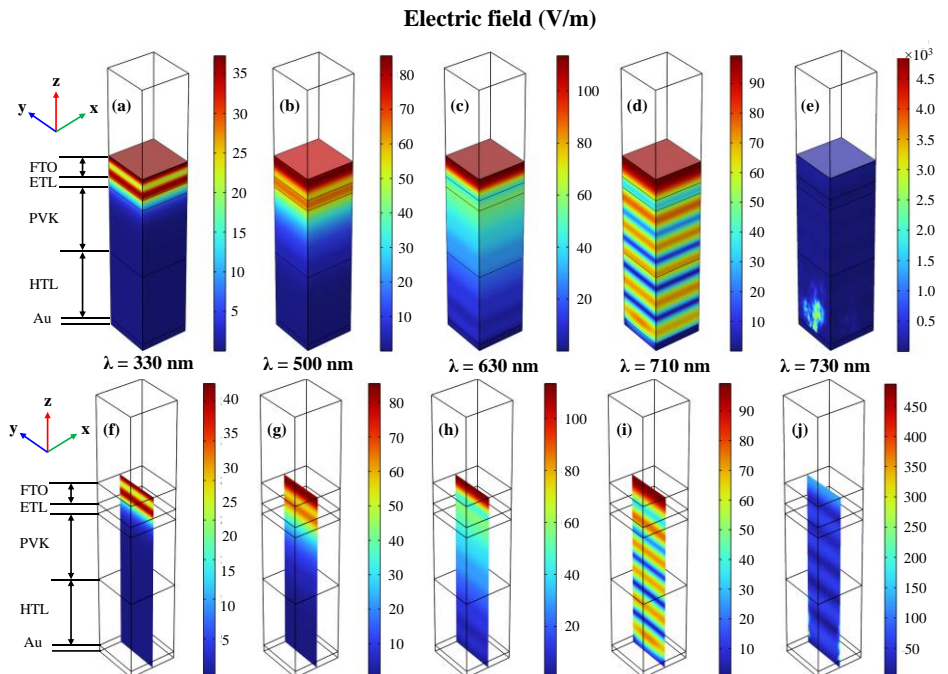


Fig. 6. (a–e) 3D and (f–j) corresponding two-dimensional (2D) cross-sectional distributions of the optical electric field at representative wavelengths. The 2D cross sections are taken in the yz plane at a fixed lateral position of $x = 125$ nm. Panels (a,f), (b,g), (c,h), (d,i), and (e,j) correspond to $\lambda = 330, 500, 630, 710$, and 730 nm, respectively. The color scales represent the electric-field magnitude in V/m. PVK corresponds to the absorber layer.

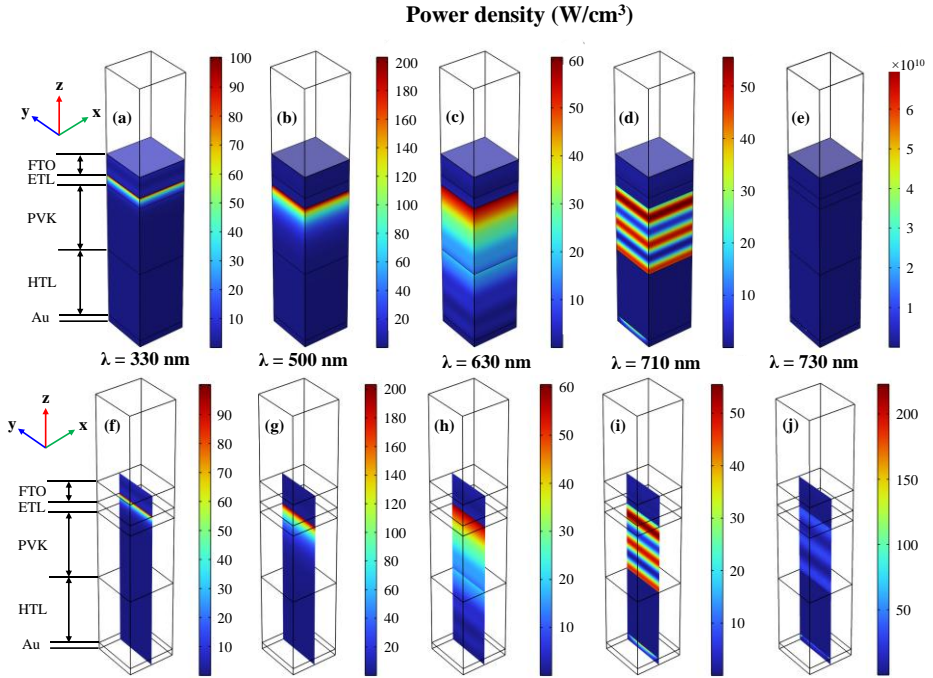


Fig. 7. (a–e) 3D and (f–j) corresponding 2D cross-sectional distributions of the local absorbed power density at representative wavelengths. The 2D cross sections are taken in the yz plane at a fixed lateral position of $x = 125$ nm. Panels (a,f), (b,g), (c,h), (d,i), and (e,j) correspond to $\lambda = 330, 500, 630, 710$, and 730 nm, respectively. The color scales represent the absorbed power density in W/cm^3 . PVK corresponds to the absorber layer.

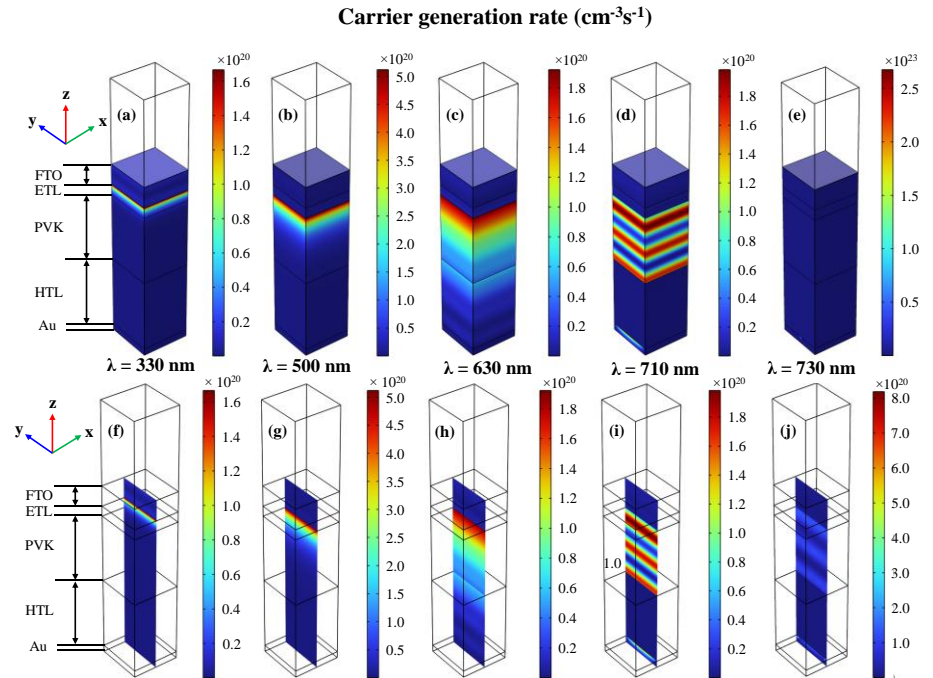


Fig. 8. (a–e) 3D and (f–j) corresponding 2D cross-sectional distributions of the carrier (electron-hole pair) generation rate at representative wavelengths. The 2D cross sections are taken in the yz plane at a fixed lateral position of $x = 125$ nm. Panels (a,f), (b,g), (c,h), (d,i), and (e,j) correspond to $\lambda = 330, 500, 630, 710$, and 730 nm, respectively. The color scales represent the generation rate in $\text{cm}^{-3}\text{s}^{-1}$. PVK corresponds to the absorber layer.

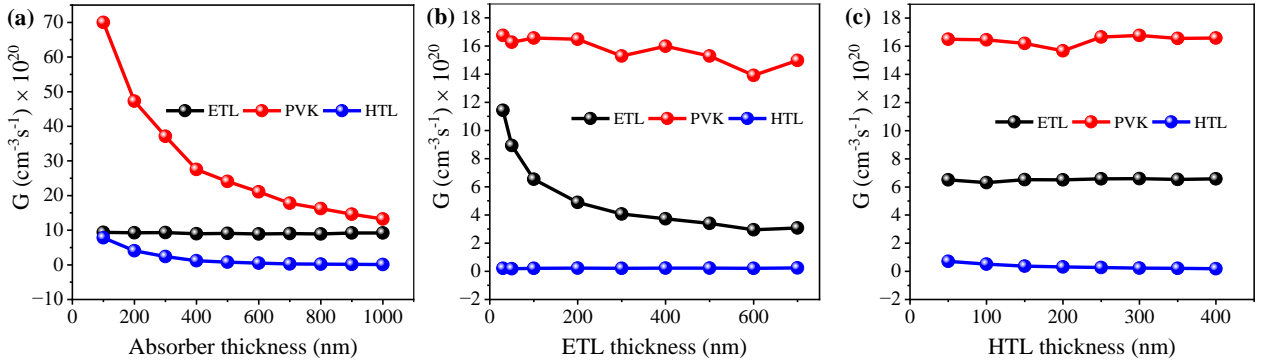


Fig. 9. Wavelength-integrated volume-averaged carrier generation rate inside the absorber (PVK in the legend), ETL, and HTL as a function of layer thickness: (a) absorber, (b) ETL, and (c) HTL. For (a), ETL and HTL thicknesses were fixed at 50 nm and 350 nm, respectively; for (b), absorber and HTL thicknesses were fixed at 800 nm and 350 nm; and for (c), absorber and ETL thicknesses were fixed at 800 nm and 100 nm.

3.3.2 Thickness-Dependent Carrier Generation in ETL, Absorber, and HTL

Following the wavelength-resolved optical analysis, the influence of individual layer thickness on the volume-averaged carrier generation rate was next examined (Fig. 9). The thicknesses of the absorber, ETL, and HTL were varied independently while keeping the remaining layers fixed, allowing the role of each layer in governing overall photogeneration to be isolated.

When the thickness of the $\text{Cs}_2\text{AgBiBr}_6$ absorber was increased, a monotonic decrease in the generation rate within the absorber was observed (Fig. 9a). This trend arises because optical absorption in $\text{Cs}_2\text{AgBiBr}_6$ is strongly front-loaded, with most photons absorbed near the ETL/absorber interface, as established by the earlier Q_{abs} and generation profiles. Increasing absorber thickness therefore enlarges the optically weakly excited rear region, reducing the average generation rate when normalized over the full absorber volume. In contrast, the generation rates within the ETL and HTL remain nearly unchanged and negligibly small, confirming that photogeneration is predominantly confined to the absorber layer and is insensitive to absorber thickness variations in the adjacent transport layers.

A similar but weaker trend is observed when varying the ETL thickness (Fig. 9b). Increasing the CeO_2 thickness from 30 nm to 700 nm leads to a slight reduction in the generation rate within the absorber, accompanied by a continuous decrease in generation within the ETL itself. The latter reflects

the dilution of absorbed power over a thicker wide-bandgap layer, while the former originates from increased optical attenuation and parasitic absorption in the ETL, which reduce photon flux reaching the absorber. Throughout this thickness range, the generation rate within the HTL remains essentially zero, signifying negligible absorption in the investigated spectral range.

In contrast, variation of the HTL thickness has a negligible influence on photogeneration within the device (Fig. 9c). As the P3HT thickness is increased from 50 to 400 nm, the carrier generation rate inside the $\text{Cs}_2\text{AgBiBr}_6$ absorber remains nearly unchanged, with only a shallow dip observed around 200 nm. The generation rate within the ETL likewise remains essentially constant, while photogeneration inside the HTL itself is negligible across the entire thickness range. These behaviors reflect the fact that photon absorption occurs predominantly within the $\text{Cs}_2\text{AgBiBr}_6$ absorber, while P3HT, owing to its wider bandgap relative to the absorber, does not contribute appreciably to absorption over the relevant spectral range. The minor reduction in generation at intermediate HTL thickness is attributed to thickness-dependent optical field redistribution within the multilayer stack, which slightly modifies the standing-wave pattern near the absorber/HTL interface rather than introducing additional parasitic absorption.

Overall, these thickness-dependent trends reinforce the earlier wavelength-resolved findings: photogeneration in the $\text{CeO}_2/\text{Cs}_2\text{AgBiBr}_6/\text{P3HT}$ architecture is dominated by absorption within the absorber and is primarily governed by optical field distribution and interference effects rather than absorption in the transport layers. Variations in ETL and HTL thickness mainly modulate the spatial redistribution of the optical field and photon flux reaching the absorber, whereas changes in absorber thickness predominantly affect the volumetric averaging of the generation rate rather than the total absorbed photon number. These thickness-dependent generation rates are fed into the Semiconductor module for the subsequent charge transport analysis, allowing a self-consistent evaluation of how optical-geometrical interplay influences device performance – an aspect often simplified or neglected in prior studies.

3.4 Electrical Performance

3.4.1 Effect of Absorber Thickness and Doping Density

To explore the influence of absorber-layer properties on overall device performance, the thickness and acceptor doping density of the $\text{Cs}_2\text{AgBiBr}_6$ absorber were varied while keeping all other structural and material parameters fixed (Fig. 10a-d). V_{OC} increases with absorber doping density for a given absorber thickness, with a noticeably stronger rate of increase beyond a doping density of approximately 10^{16} cm^{-3} (Fig. 10a). When the absorber thickness is varied, V_{OC} increases only weakly at low doping densities ($\leq 10^{16} \text{ cm}^{-3}$), whereas a more pronounced thickness-dependent enhancement is observed for highly doped absorbers. These trends originate from the evolution of band bending and quasi-Fermi level splitting within the absorber. At low doping densities, weak internal electric fields limit the potential that can be sustained across the absorber, so increasing thickness primarily extends the quasi-neutral region and has little impact on V_{OC} . With increasing doping density, stronger band bending at both the $\text{CeO}_2/\text{Cs}_2\text{AgBiBr}_6$ and $\text{Cs}_2\text{AgBiBr}_6/\text{P3HT}$ interfaces enhances field-assisted carrier separation

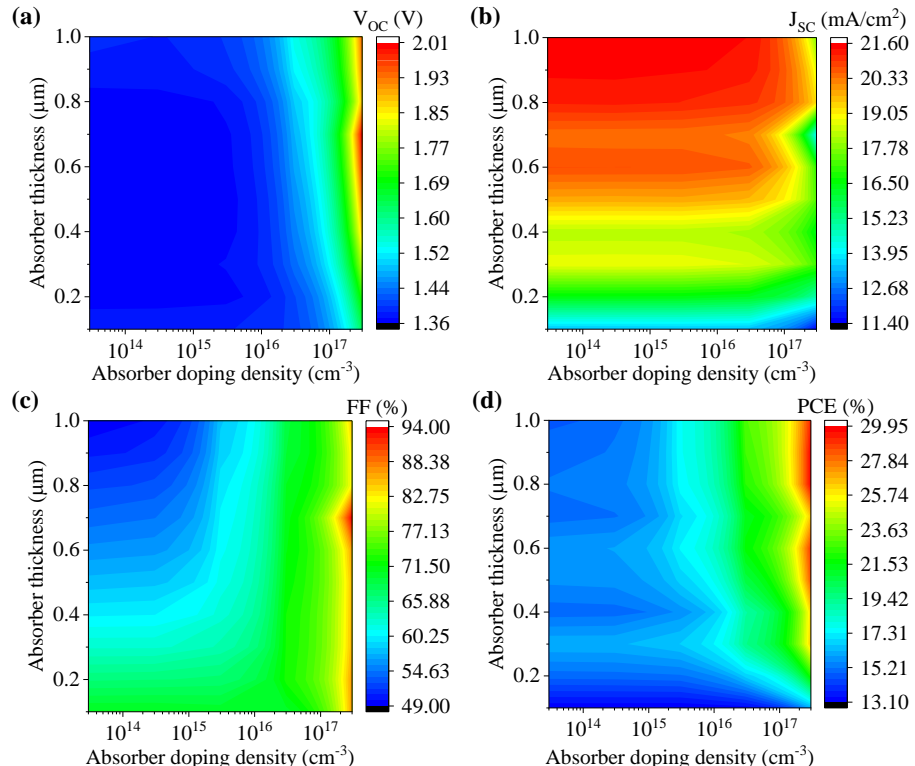


Fig. 10. Effect of thickness and doping density of the absorber, $\text{Cs}_2\text{AgBiBr}_6$ on V_{OC} , J_{SC} , FF, and PCE of the device. All other material parameters were kept fixed at their default values (Tables 1-3).

and suppresses recombination, allowing quasi-Fermi level splitting to be maintained deeper into the absorber and resulting in a stronger thickness dependence of V_{OC} .

J_{SC} exhibits more complex dependencies (Fig. 10b). For a fixed absorber thickness, J_{SC} remains nearly independent of doping density up to approximately $3 \times 10^{16} \text{ cm}^{-3}$ and decreases at higher doping levels. With increasing absorber thickness, J_{SC} increases at low and moderate doping densities due to enhanced optical absorption, while at the highest doping density studied in this work ($3 \times 10^{17} \text{ cm}^{-3}$), a non-monotonic thickness dependence is observed, characterized by an initial increase followed by a reduction at intermediate thickness and partial recovery at larger thicknesses. These behaviors reflect the competition between absorption-driven current enhancement and doping-induced recombination losses. At high doping densities, increased free-carrier concentration and defect-assisted recombination shorten carrier lifetimes, reducing current collection efficiency, particularly in thicker absorbers where carriers need to traverse longer transport paths.

For a fixed thickness, FF remains nearly constant with increasing doping density up to approximately $3 \times 10^{14} \text{ cm}^{-3}$ and increases thereafter (Fig. 10c). When absorber thickness is varied, FF generally decreases with thickness, with the reduction being more pronounced at low doping densities and becoming weaker at higher doping levels. At the highest doping density, FF exhibits a sharp enhancement at an intermediate thickness ($\sim 0.7 \mu\text{m}$), followed by degradation at larger thicknesses. These trends arise from the interplay between series resistance, recombination, and field-assisted carrier extraction. At low doping densities, limited conductivity leads to increased transport resistance and carrier accumulation in thicker absorbers, reducing FF. Increasing doping density improves absorber conductivity and strengthens the internal electric field, reducing resistive losses and enabling more efficient carrier extraction, which explains the FF enhancement and its partial recovery at high doping and intermediate thickness.

PCE reflects the combined evolution of V_{OC} , J_{SC} , and FF with absorber doping density and thickness (Fig. 10d). For a given thickness, PCE remains nearly constant at low doping densities and increases at higher doping levels, with the onset of improvement occurring at lower doping densities for thicker absorbers. When absorber thickness is varied, PCE generally increases with thickness, and the rate of enhancement becomes more pronounced at higher doping densities. These trends result from the balance between voltage enhancement, photocurrent generation, and fill-factor evolution. At low doping densities, thickness-induced absorption gains are partially offset by transport and recombination losses, limiting PCE improvement. At higher doping densities, stronger internal electric fields and improved conductivity allow thickness-related absorption gains to translate more effectively into increases in efficiency.

3.4.2 Effect of ETL Thickness and Doping Density

Following the absorber-layer analysis, the role of the ETL was examined by varying the thickness and donor doping density of the CeO_2 ETL while maintaining all other device parameters constant (Fig. 11a-d). For thick ETLs ($> 0.5 \mu\text{m}$), V_{OC} increases with ETL doping density for a given thickness, with the enhancement becoming pronounced once the doping density exceeds approximately 10^{18} cm^{-3} (Fig. 11a). The increase continues up to $\sim 2 \times 10^{20} \text{ cm}^{-3}$, beyond which a reduction in V_{OC} is observed. For thin ETLs ($\leq 0.5 \mu\text{m}$), V_{OC} remains nearly constant with ETL doping density up to $2 \times 10^{19} \text{ cm}^{-3}$, followed by a noticeable increase at $2 \times 10^{20} \text{ cm}^{-3}$ and a slight degradation at higher doping densities. When ETL thickness is varied, V_{OC} increases with thickness up to approximately $0.5 \mu\text{m}$ for all doping densities. Beyond this thickness, V_{OC} decreases at low ETL doping densities ($\leq 10^{17} \text{ cm}^{-3}$), whereas it continues to increase for highly doped ETLs ($\geq 10^{18} \text{ cm}^{-3}$).

These trends originate from the evolution of band bending, electron selectivity, and recombination at the $\text{CeO}_2/\text{Cs}_2\text{AgBiBr}_6$ interface. At low ETL doping densities, weak band bending and limited electron conductivity reduce the internal electric field and increase interfacial recombination, so increasing ETL

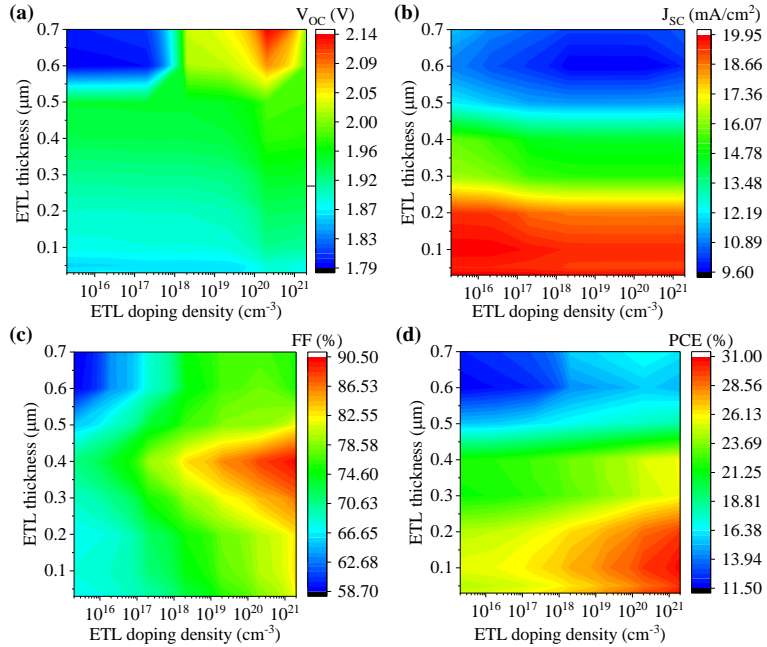


Fig. 11. Effect of thickness and doping density of the ETL (CeO_2) on V_{OC} , J_{SC} , FF, and PCE of the device. The absorber thickness and acceptor doping density were fixed at 800 nm and $3 \times 10^{17} \text{ cm}^{-3}$, respectively, which yielded the maximum PCE in section 3.4.1. All other material parameters were kept fixed at their default values (Tables 1-3).

thickness beyond an optimal value primarily introduces transport resistance and recombination losses, leading to reduced V_{OC} . As ETL doping density increases, stronger band bending enhances electron selectivity and suppresses carrier backflow into the absorber, allowing quasi-Fermi level splitting to be preserved across thicker ETLs and resulting in a stronger thickness-dependent enhancement of V_{OC} . At excessively high doping densities, increased free-carrier concentration and defect-assisted recombination within the ETL counteract these benefits, producing the observed reduction in V_{OC} .

J_{SC} exhibits a comparatively weak dependence on ETL doping density (Fig. 11b). For a fixed ETL thickness, J_{SC} remains nearly independent of ETL doping over most of the investigated range, with only slight reductions observed at high doping densities when the ETL is thick. The maximum variation corresponds to a decrease from approximately 15.84 to 14.5 mA cm^{-2} at an ETL thickness of $0.4 \mu\text{m}$. This limited variation indicates that photocurrent generation is primarily governed by optical absorption in the $\text{Cs}_2\text{AgBiBr}_6$ absorber rather than by ETL electronic properties. When ETL thickness is varied, J_{SC} decreases monotonically with increasing thickness, primarily due to enhanced parasitic absorption and increased transport resistance in the CeO_2 layer, which limit carrier extraction.

FF increases monotonically with ETL doping density for all ETL thicknesses studied (Fig. 11c). When ETL thickness is varied, FF increases up to an intermediate thickness of approximately $0.4 \mu\text{m}$ and decreases at larger thicknesses.

These trends arise from the interplay between series resistance, recombination, and field-assisted carrier extraction. Increasing ETL doping density enhances electron conductivity and reduces series resistance, facilitating more efficient carrier extraction and improving FF. Moderate increases in ETL thickness improve junction uniformity and reduce leakage pathways, resulting in initial FF enhancement. Beyond the optimal thickness, however, increased transport resistance and carrier accumulation dominate, leading to FF degradation despite improved ETL conductivity.

For a given ETL thickness, PCE increases monotonically with ETL doping density (Fig. 11d). When ETL thickness is varied, PCE exhibits a non-linear dependence, characterized by an initial decrease at low and moderate thicknesses, followed by a partial recovery at larger thicknesses.

These trends result from the balance between voltage enhancement, photocurrent collection, and fill-factor evolution. At small ETL thicknesses, efficiency gains are obtained due to reduced series resistance and enhanced junction selectivity. As ETL thickness increases, losses in J_{SC} associated with parasitic absorption and transport resistance outweigh gains in V_{OC} , leading to PCE degradation. At very large ETL thicknesses and high doping densities, strengthened band bending and improved electron selectivity partially compensate for current losses, resulting in the observed recovery in PCE.

3.4.3 Effect of HTL Thickness and Doping Density

Similarly, the influence of HTL properties on device performance was investigated by independently varying the thickness and acceptor doping density of the P3HT HTL while keeping all other parameters fixed (Fig. 12a–d). V_{OC} increases monotonically with HTL doping density for all HTL thicknesses studied, with a noticeably stronger rate of increase at larger HTL thicknesses ($\geq 0.35 \mu\text{m}$) (Fig. 12a). When HTL thickness is varied, V_{OC} exhibits a non-monotonic dependence: it increases initially up to $\sim 0.1 \mu\text{m}$, decreases slightly at $\sim 0.15 \mu\text{m}$, rises again up to $\sim 0.3 \mu\text{m}$, followed by a reduction at $\sim 0.35 \mu\text{m}$ and a subsequent recovery at larger thicknesses.

These trends originate from the evolution of band bending, hole selectivity, and interfacial recombination at the $\text{Cs}_2\text{AgBiBr}_6/\text{P3HT}$ interface. At low HTL doping densities, limited hole conductivity and weak band bending restrict efficient hole extraction, making V_{OC} sensitive to thickness-induced transport losses. Increasing HTL doping strengthens band bending and improves

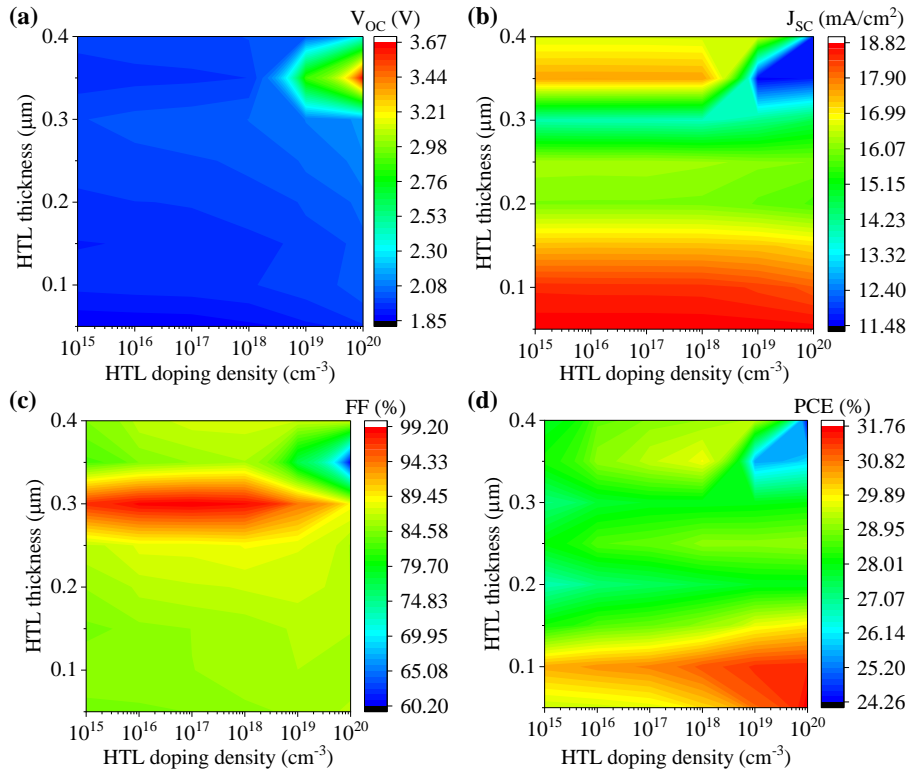


Fig. 12. Effect of thickness and doping density of the HTL (P3HT) on V_{OC} , J_{SC} , FF, and PCE of the device. The absorber and ETL thicknesses were fixed at 800 nm and 100 nm respectively, while their acceptor and donor doping densities were maintained at $3 \times 10^{17} \text{ cm}^{-3}$ and $2 \times 10^{21} \text{ cm}^{-3}$, respectively, which yielded the maximum PCE in section 3.4.2. All other material parameters were kept fixed at their default values (Tables 1–3).

hole selectivity, suppressing interfacial recombination and allowing quasi-Fermi level splitting to be better preserved, particularly in thicker HTLs. The non-monotonic thickness dependence reflects the competing effects of improved junction formation at moderate thicknesses and increased transport resistance and carrier accumulation in thicker P3HT layers. At sufficiently large thicknesses, improved interface quality and stabilized band alignment partially offset transport losses, leading to V_{OC} recovery.

J_{SC} shows a comparatively weak dependence on HTL doping density (Fig. 12b). For HTL thicknesses up to $\sim 0.3 \mu\text{m}$, J_{SC} remains nearly independent of doping density, whereas a reduction is observed at higher doping levels ($\geq 10^{19} \text{ cm}^{-3}$) when the HTL is thick ($\geq 0.35 \mu\text{m}$). When HTL thickness is varied, J_{SC} generally decreases with increasing thickness; however, a noticeable recovery in J_{SC} occurs at larger thicknesses ($\geq 0.3 \mu\text{m}$) when doping density is $\leq 10^{19} \text{ cm}^{-3}$.

This behavior indicates that photocurrent generation is primarily governed by optical absorption in the $\text{Cs}_2\text{AgBiBr}_6$ absorber, while charge extraction is limited by hole transport in the P3HT layer. The initial reduction in J_{SC} with HTL thickness arises from increased transport resistance and carrier accumulation in thicker layers, which enhance recombination losses. At intermediate doping densities, improved hole conductivity and reduced interfacial recombination partially mitigate these losses at larger thicknesses, leading to the observed recovery in J_{SC} .

FF exhibits a moderate dependence on both HTL doping density and thickness (Fig. 12c). For thin HTLs ($\leq 0.25 \mu\text{m}$), FF increases slightly with increasing doping density. At higher thicknesses ($0.3\text{--}0.35 \mu\text{m}$), FF decreases beyond a doping density of $\sim 10^{18} \text{ cm}^{-3}$, whereas at the largest thickness studied ($0.4 \mu\text{m}$), FF shows saturation at high doping densities following an initial increase. When thickness is varied, FF increases up to $\sim 0.3 \mu\text{m}$, decreases at $\sim 0.35 \mu\text{m}$, and increases again at larger thicknesses.

These trends reflect the balance between series resistance, recombination, and junction uniformity. Moderate increases in HTL thickness improve interfacial coverage and suppress shunt pathways, enhancing FF. However, thicker P3HT layers introduce higher transport resistance and carrier accumulation, leading to FF degradation at intermediate thicknesses. Increasing HTL doping improves hole conductivity and reduces resistive losses, stabilizing FF at large thicknesses and producing saturation behavior at high doping densities.

For HTL thicknesses $\leq 0.3 \mu\text{m}$, PCE increases slightly with doping density, whereas at larger thicknesses ($\geq 0.35 \mu\text{m}$), a reduction in PCE is observed at high doping densities ($\geq 10^{18} \text{ cm}^{-3}$) (Fig. 12d). When HTL thickness is varied, PCE exhibits a strongly non-monotonic behavior, characterized by alternating regions of enhancement and degradation.

At small HTL thicknesses, efficiency improvements are driven mainly by the improved hole selectivity and reduced series resistance. As thickness increases, J_{SC} losses associated with transport resistance and recombination dominate, reducing PCE. At specific thickness–doping combinations, partial recovery occurs when improved junction quality and stabilized band alignment compensate for transport limitations.

3.4.4 Effect of Absorber Defect Density

Prior experimental and theoretical studies have identified a diverse population of defect species in $\text{Cs}_2\text{AgBiBr}_6$, including halide vacancies (V_{Br}), cation vacancies ($V_{\text{Ag}}, V_{\text{Bi}}$), and antisite defects (e.g., $\text{Ag}_{\text{Bi}}, \text{Bi}_{\text{Ag}}$) that introduce trap states within the bandgap and act as non-radiative recombination centers [71], [72]. Therefore, the absorber bulk defect density was treated as a key variable in the present study and varied from 10^{12} to 10^{18} cm^{-3} to explore the impact on device performance (Fig. 13). All the photovoltaic parameters exhibit a monotonic degradation with increasing defect density. At relatively low defect concentrations ($\leq 10^{14} \text{ cm}^{-3}$), the parameters decrease only gradually, indicating that non-

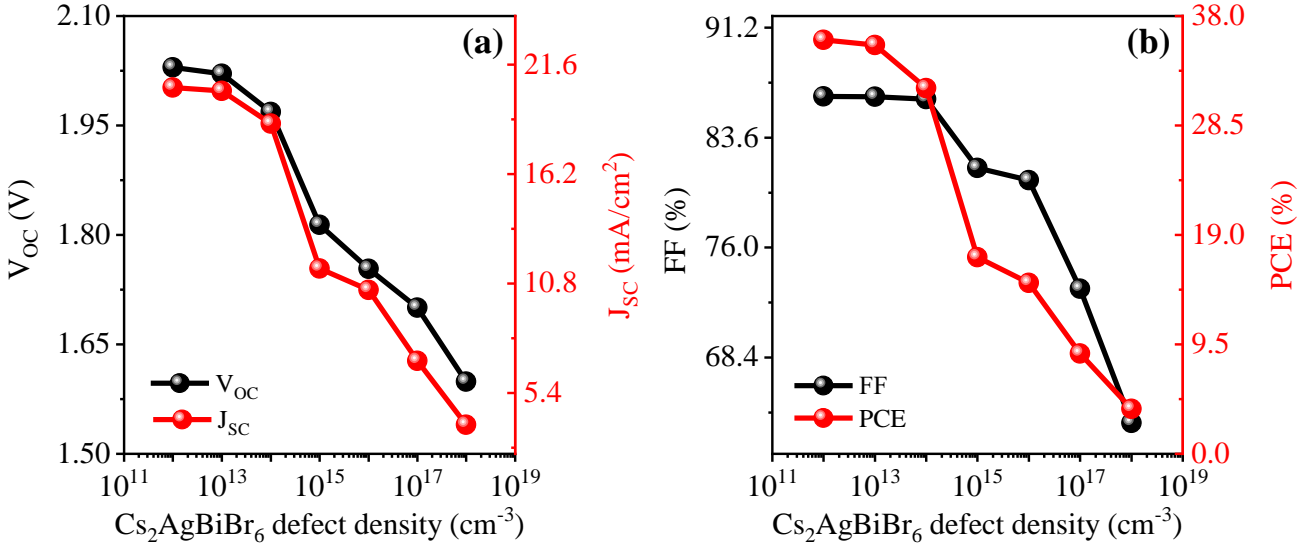


Fig. 13. Effect of bulk defect density in the $\text{Cs}_2\text{AgBiBr}_6$ on V_{OC} , J_{SC} , FF, and PCE of the device. The absorber, ETL and HTL thicknesses were fixed at 800 nm, 100 nm and 50 nm, respectively, while their doping densities were maintained at $3 \times 10^{17} \text{ cm}^{-3}$, $2 \times 10^{21} \text{ cm}^{-3}$ and 10^{20} cm^{-3} , respectively, which yielded the maximum PCE in section 3.4.3. All other material parameters were kept fixed at their default values (Tables 1-3).

radiative recombination remains weak and does not yet dominate the overall carrier dynamics. However, once the defect density reaches $\sim 10^{15} \text{ cm}^{-3}$ and above, device performance degrades rapidly across all key metrics.

This transition reflects the onset of defect-assisted SRH recombination as the dominant recombination pathway within the absorber. As the defect density (N_t) increases, the carrier lifetimes (τ_n and τ_p) and diffusion lengths (L_n and L_p) are significantly reduced (equation 21-22, [73]), leading to enhanced non-radiative recombination within the absorber.

$$\tau_{n,p} = \frac{1}{\sigma_{n,p} N_t v_{th}} \quad (21)$$

$$L_{n,p} = \sqrt{\frac{kT}{q} \mu_{n,p} \tau_{n,p}} \quad (22)$$

where σ is the carrier capture cross-section, and v_{th} is the thermal velocity. The resulting reduction in $\tau_{n,p}$ and $L_{n,p}$ directly suppresses the quasi-Fermi level splitting, giving rise to a rapid decline in V_{OC} . Simultaneously, intensified bulk recombination reduces the collection probability of photogenerated carriers, causing a measurable decrease in J_{SC} . FF is also adversely affected at high defect densities, as increased recombination near the maximum power point degrades diode ideality and flattens the J-V characteristics. As a cumulative outcome of these losses, the PCE deteriorates sharply beyond the critical defect density threshold.

Overall, these results suggest that maintaining defect concentrations below $\sim 10^{14} \text{ cm}^{-3}$ is essential to preserve long carrier lifetimes, efficient charge extraction, and high photovoltaic performance in the device.

3.4.5 Effect of CTL/Absorber Interface Defect Density

In addition to bulk defects, defects at the $\text{CeO}_2/\text{Cs}_2\text{AgBiBr}_6$ and $\text{P3HT}/\text{Cs}_2\text{AgBiBr}_6$ interfaces can significantly influence device performance. These interface defects primarily originate from interfacial

disorder, surface roughness, imperfect band alignment, and incomplete chemical passivation during layer deposition. They act as recombination centers and are commonly described within the SRH formalism through an interface recombination velocity, reflecting their critical influence on carrier extraction and voltage losses.

For an interface defect density N_{it} , the SRH interface recombination rate can be expressed as

$$R_{int} = \frac{S_n S_p (n_p - n_i^2)}{S_n (n + n_1) + S_p (p + p_1)} \quad (23)$$

$$n_1 = n_i \exp\left(\frac{E_t - E_i}{kT}\right), \quad p_1 = n_i \exp\left(\frac{E_i - E_t}{kT}\right) \quad (24)$$

where $S_n = \sigma_n v_{th} N_{it}$ and $S_p = \sigma_p v_{th} N_{it}$ are the electron and hole interface recombination velocities, respectively, σ denotes the capture cross section, E_t is the energy level of the interface trap, E_i is the intrinsic Fermi level, n_i is the intrinsic carrier concentration, k is the Boltzmann constant and T is the temperature. An increase in N_{it} therefore enhances interface recombination and reduces carrier lifetimes near the interface.

3.4.5.1 ETL/Absorber Interface Defect

V_{OC} shows a weakly non-monotonic dependence on $\text{CeO}_2/\text{Cs}_2\text{AgBiBr}_6$ interface defect density (Fig. 14). A slight increase in V_{OC} is observed at very low interface defect densities (5×10^7 – $1 \times 10^8 \text{ cm}^{-2}$) (Fig. 14a). Within the numerical model, this behavior is attributed to minor electrostatic redistribution and changes in local quasi-Fermi level splitting under extremely low interface recombination conditions, rather than to an explicit interface passivation effect. Beyond this narrow regime, at higher defect densities, V_{OC} decreases gradually as enhanced SRH recombination at the interface reduces the quasi-Fermi level splitting.

J_{SC} decreases monotonically with increasing defect density, although the total reduction remains small ($\sim 0.5\%$ up to $5 \times 10^{12} \text{ cm}^{-2}$) (Fig. 14a). This weak sensitivity indicates that electron extraction through CeO_2 is comparatively resilient to moderate interface recombination. Under short-circuit conditions, carrier collection is dominated by field-assisted transport and favorable conduction-band alignment at

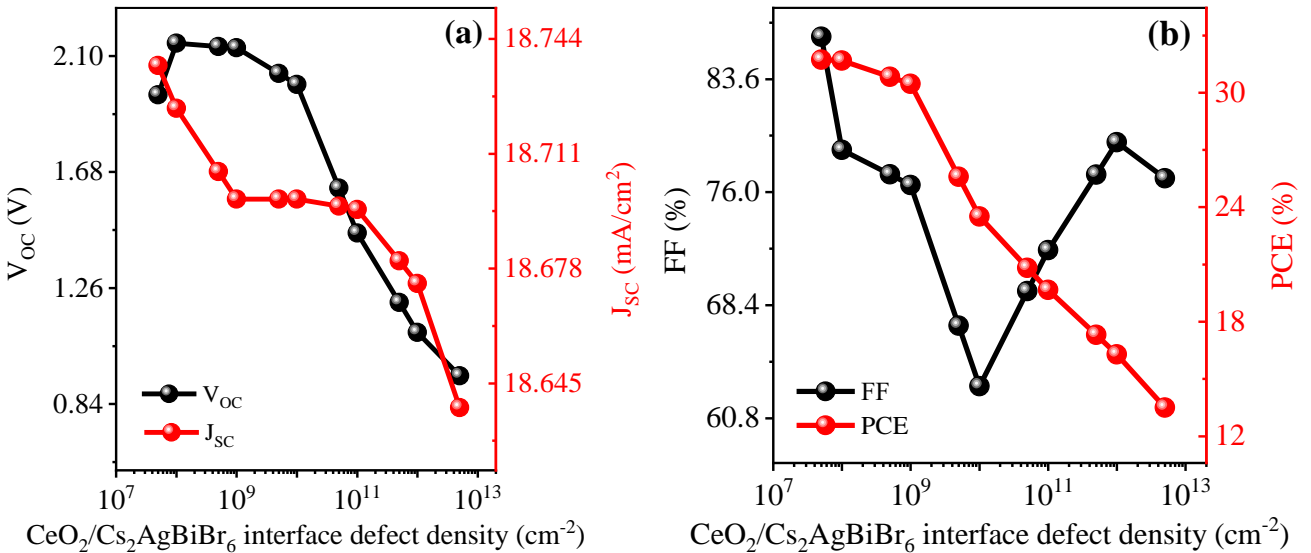


Fig. 14. Effect of defect density at $\text{CeO}_2/\text{Cs}_2\text{AgBiBr}_6$ interface on V_{OC} , J_{SC} , FF, and PCE of the device. The absorber, ETL and HTL thicknesses were fixed at 800 nm, 100 nm and 50 nm, respectively, while their doping densities were maintained at $3 \times 10^{17} \text{ cm}^{-3}$, $2 \times 10^{21} \text{ cm}^{-3}$ and 10^{20} cm^{-3} , respectively, which yielded the maximum PCE in section 3.4.3. All other material parameters were kept fixed at their default values (Tables 1-3).

the $\text{CeO}_2/\text{Cs}_2\text{AgBiBr}_6$ interface, which promote rapid carrier sweep-out and limit the residence time of electrons near interfacial recombination centers.

FF displays a more complex response (Fig. 14b). FF initially decreases with increasing interface defect density up to approximately 10^{10} cm^{-2} , reflecting enhanced recombination losses near the maximum power point. Interestingly, a partial recovery in FF is observed at intermediate defect densities, before a renewed decline occurs once the defect density exceeds 10^{12} cm^{-2} . This non-monotonic trend suggests a competition between recombination-induced losses and changes in interfacial charge transport, where moderate defect densities may transiently modify local electric fields or carrier selectivity, while high defect densities ultimately dominate through recombination-driven degradation.

As a cumulative consequence of these effects, the PCE decreases continuously with increasing ETL/absorber interface defect density (Fig. 14b), confirming that interface recombination at the electron-extraction side progressively undermines device performance.

3.4.5.2 HTL/Absorber Interface Defect

In contrast, defects at the $\text{P3HT}/\text{Cs}_2\text{AgBiBr}_6$ interface exert a stronger influence on device performance (Fig. 15). V_{OC} decreases steadily with increasing defect density and saturates beyond $\sim 10^{11} \text{ cm}^{-2}$ (Fig. 15a), consistent with recombination-limited quasi-Fermi level splitting once interface SRH recombination dominates.

J_{SC} also decreases with increasing defect density, with a pronounced drop emerging once the interface defect density reaches $5 \times 10^{12} \text{ cm}^{-2}$ (Fig. 15a). The reduction in J_{SC} is attributed to enhanced trap-assisted recombination at the $\text{P3HT}/\text{Cs}_2\text{AgBiBr}_6$ interface, where photogenerated holes accumulate under operation, increasing their residence time near interfacial defect states and suppressing efficient carrier extraction.

FF follows a non-monotonic trend, exhibiting an initial decline at low defect densities, a weak recovery at intermediate densities, and a sharp degradation beyond $\sim 10^{12} \text{ cm}^{-2}$ (Fig. 15b). At high defect concentrations, enhanced interface recombination significantly distorts the diode ideality and increases recombination losses near the maximum power point.

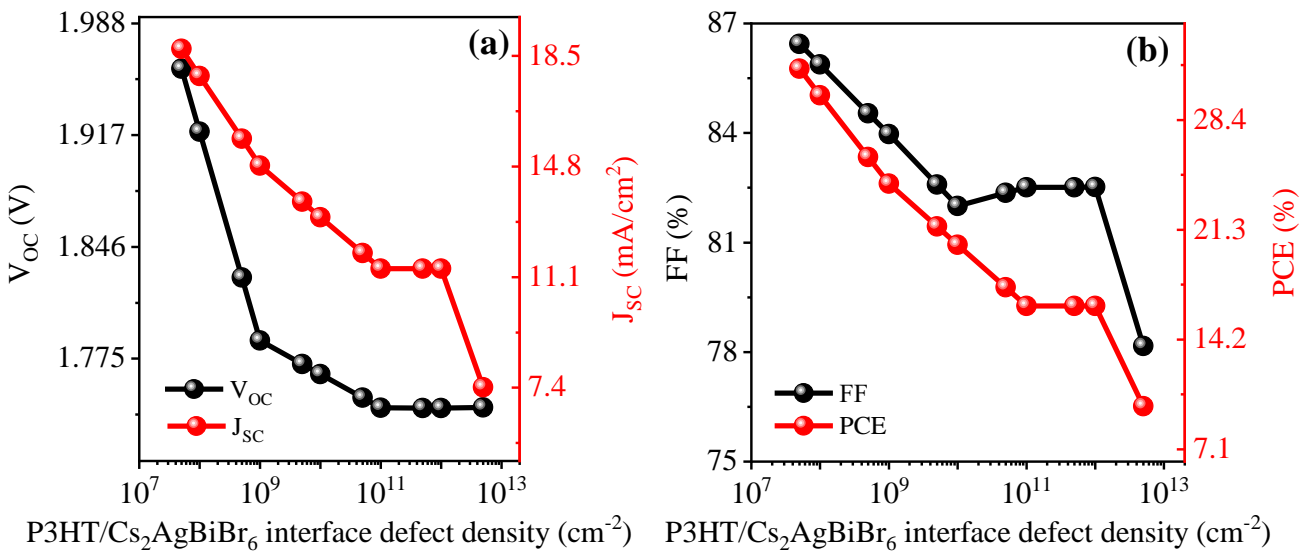


Fig. 15. Effect of defect density at $\text{P3HT}/\text{Cs}_2\text{AgBiBr}_6$ interface on V_{OC} , J_{SC} , FF, and PCE of the device. The absorber, ETL and HTL thicknesses were fixed at 800 nm, 100 nm and 50 nm, respectively, while their doping densities were maintained at $3 \times 10^{17} \text{ cm}^{-3}$, $2 \times 10^{21} \text{ cm}^{-3}$ and 10^{20} cm^{-3} , respectively, which yielded the maximum PCE in section 3.4.3. All other material parameters were kept fixed at their default values (Tables 1-3).

Consequently, the PCE decreases with increasing HTL/absorber interface defect density (Fig. 15b), remaining nearly constant only over a narrow intermediate regime before undergoing a sharp decline at high defect densities.

The results of this section highlight that effective control of interfacial defect densities is a key requirement for maintaining efficient carrier extraction and achieving high-performance $\text{Cs}_2\text{AgBiBr}_6$ -based solar cells.

3.4.6 Effect of Direct and Auger Recombination Coefficient

When the radiative (direct) and Auger recombination coefficients of the $\text{Cs}_2\text{AgBiBr}_6$ absorber are varied simultaneously, a clear threshold-dependent degradation of device performance is observed (Fig. 16). For low recombination coefficients, all photovoltaic parameters remain nearly unchanged, indicating that recombination losses are not rate-limiting in this regime. However, once either recombination coefficient increases beyond a critical level, a pronounced deterioration in device performance occurs.

At low radiative and Auger recombination coefficients, photogenerated carriers in the $\text{Cs}_2\text{AgBiBr}_6$ absorber possess sufficiently long lifetimes to be efficiently separated and extracted by the built-in electric fields at the $\text{CeO}_2/\text{Cs}_2\text{AgBiBr}_6$ and $\text{Cs}_2\text{AgBiBr}_6/\text{P3HT}$ interfaces. Under these conditions, quasi-Fermi level splitting is well preserved, leading to high V_{OC} , while efficient carrier collection sustains both J_{SC} and FF.

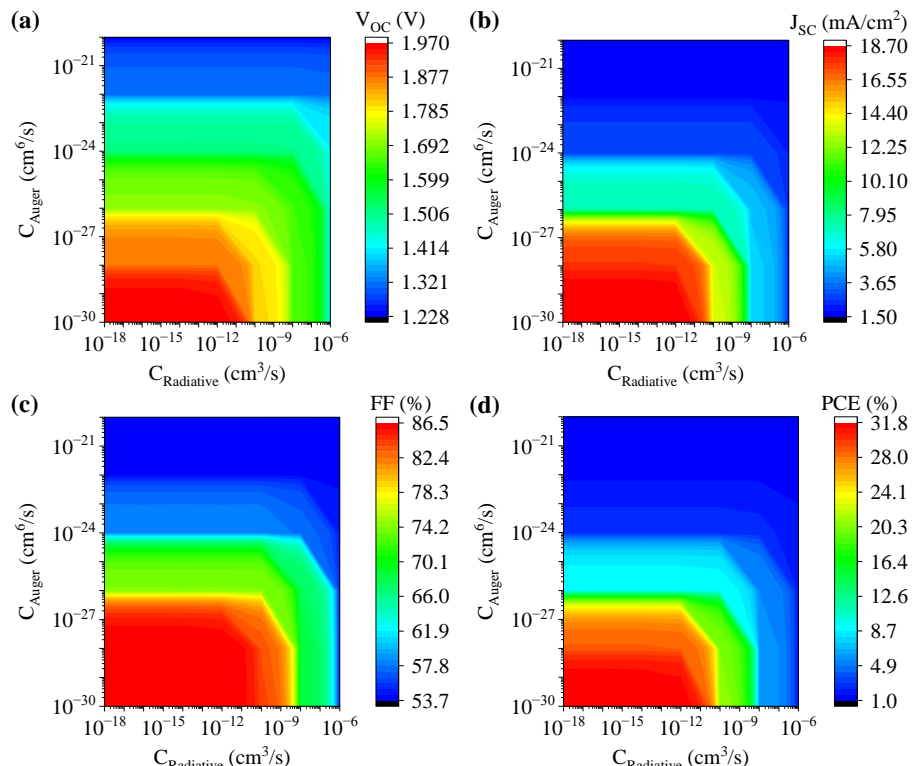


Fig. 16. Effect of radiative and Auger recombination coefficients on V_{OC} , J_{SC} , FF, and PCE of the device. All other material parameters were kept fixed at their default values (Tables 1-3), and the Auger coefficients were assumed identical for electrons and holes. The absorber, ETL and HTL thicknesses were fixed at 800 nm, 100 nm and 50 nm, respectively, while their doping densities were maintained at $3 \times 10^{17} \text{ cm}^{-3}$, $2 \times 10^{21} \text{ cm}^{-3}$ and 10^{20} cm^{-3} , respectively, which yielded the maximum PCE in section 3.4.3. All other material parameters were kept fixed at their default values (Tables 1-3).

As the radiative recombination coefficient increases beyond its threshold, band-to-band recombination losses become significant. Although radiative recombination is an intrinsic process, an excessively high radiative coefficient reduces the effective carrier lifetime and limits the achievable quasi-Fermi level splitting, resulting in a noticeable reduction in V_{OC} (Fig. 16a). The accompanying increase in bulk recombination also lowers carrier collection efficiency, contributing to simultaneous declines in J_{SC} and FF (Fig. 16b,c).

Auger recombination has an even more detrimental impact at higher carrier densities due to its strong dependence on carrier concentration. Once the Auger recombination coefficient exceeds $\sim 10^{-29} \text{ cm}^6 \text{ s}^{-1}$, three-carrier recombination processes dominate, particularly in regions of strong band bending near the junction where carrier densities are highest. This leads to rapid carrier annihilation, severely reducing carrier lifetime and diffusion length. As a consequence, the performance parameters degrade markedly.

The cumulative effect of these recombination losses is clearly reflected in the PCE (Fig. 16d). PCE exhibits a pronounced decline once either recombination coefficient exceeds its critical threshold. Based on the observed trends, optimal device performance is achieved when the radiative recombination coefficient remains below $\sim 10^{-11} \text{ cm}^3 \text{ s}^{-1}$ and the Auger recombination coefficient remains below $\sim 10^{-29} \text{ cm}^6 \text{ s}^{-1}$.

3.4.7 Effect of Temperature

The temperature dependence of the photovoltaic performance of the device was investigated over a wide temperature range from 200 to 500 K to assess the interplay between thermal activation, charge transport, and recombination (Fig. 17). All device metrics exhibit non-monotonic temperature dependence, indicating a transition between transport-limited and recombination-limited operating regimes.

V_{OC} initially increases with temperature up to approximately 300 K, followed by a gradual decrease up to ~ 350 K and saturation at higher temperatures. This behavior is consistent with the temperature dependence of the quasi-Fermi level splitting (equation 16). At low temperatures (200–300 K), enhanced thermal activation of the carriers and reduced interfacial barriers lead to a positive temperature coefficient, $\left(\frac{dV_{OC}}{dT}\right)_{T<300K} > 0$. At higher temperatures, the exponential increase of J_0 dominates [74],

$$J_0 \propto T^3 \exp\left(-\frac{E_g}{kT}\right) \quad (25)$$

resulting in a negative temperature coefficient, $\left(\frac{dV_{OC}}{dT}\right)_{T>300K} < 0$, as recombination and effective bandgap narrowing reduce the attainable voltage. The eventual saturation of V_{OC} above ~ 350 K indicates a recombination-controlled regime in which further thermal activation no longer alters the quasi-Fermi level splitting.

J_{SC} shows a similarly non-monotonic temperature dependence. J_{SC} increases slightly from 200 K to ~ 275 K due to enhanced carrier mobility and improved charge collection efficiency. With further temperature increase up to ~ 325 K, J_{SC} decreases as carrier–phonon scattering and thermally activated recombination increasingly limit carrier transport. At higher temperatures, J_{SC} becomes nearly

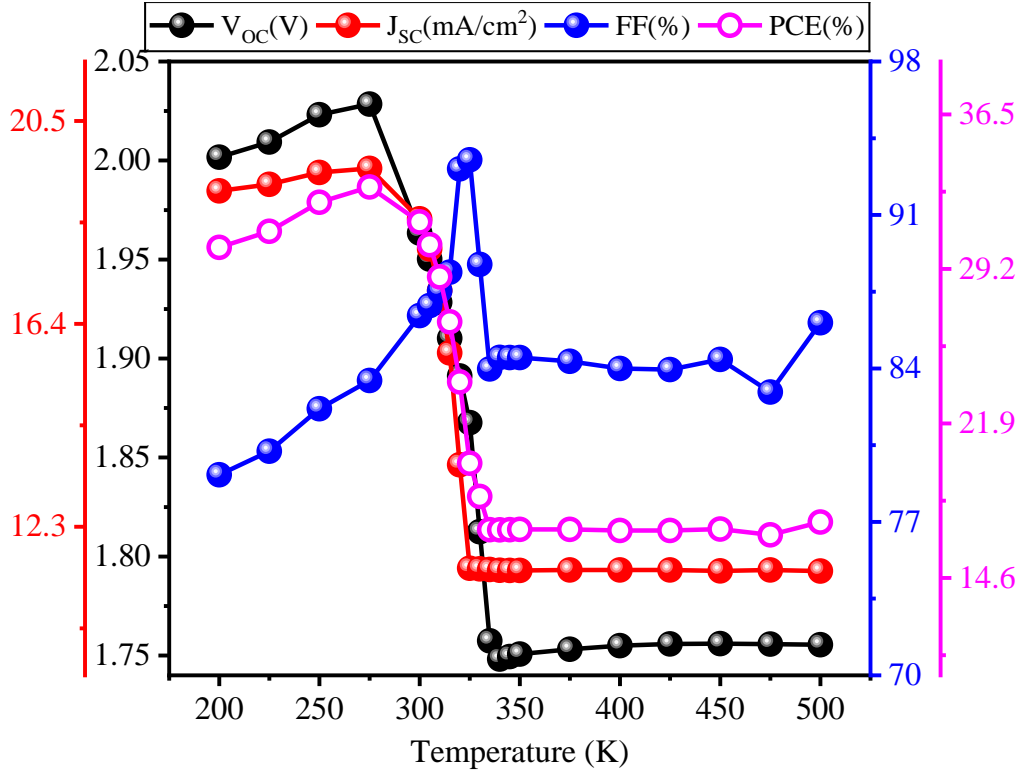


Fig. 17. Effect of temperature (T) on V_{oc} , J_{sc} , FF, and PCE of the device. The absorber, ETL and HTL thicknesses were fixed at 800 nm, 100 nm and 50 nm, respectively, while their doping densities were maintained at 3×10^{17} cm⁻³, 2×10^{21} cm⁻³ and 10^{20} cm⁻³, respectively, which yielded the maximum PCE in section 3.4.3. All other material parameters were kept fixed at their default values (Tables 1-3).

temperature independent, suggesting that optical generation and transport losses reach a dynamic balance that is weakly sensitive to further thermal variation.

FF shows an initial improvement with temperature, reaching a maximum near ~325 K, followed by a gradual decline at higher temperatures and eventual saturation above ~350 K. The initial increase in FF can be attributed to reduced series resistance and improved carrier transport with increasing temperature. At higher temperatures, however, increased recombination and enhanced resistive losses reduce the squareness of the current–voltage characteristics, leading to FF degradation.

As the cumulative metric, PCE closely tracks the combined evolution of V_{oc} , J_{sc} , and FF. PCE increases initially with temperature, reaching a maximum near ~275 K, driven by the simultaneous enhancement of V_{oc} , a modest increase in J_{sc} , and improved FF. At higher temperatures, the concurrent reduction in V_{oc} and J_{sc} dominates, resulting in a progressive decrease in PCE up to ~340 K, followed by a plateau at higher temperatures. This saturation reflects the establishment of a thermally limited operating regime in which further increases in temperature do not substantially alter the balance between photogeneration, transport, and recombination.

Overall, the temperature-dependent behavior underscores the critical role of thermally activated recombination in limiting device performance at elevated temperatures, while also highlighting an optimal operating window near room temperature where transport, recombination, and interfacial energetics are most favorably balanced in the device.

3.4.8 Effect of Incident Light Intensity

The operational response of the device under varying illumination conditions was evaluated by examining the dependence of the photovoltaic parameters on incident light intensity (Fig. 18), an essential consideration given the substantial fluctuations in irradiance between outdoor and indoor environments and under different weather conditions. V_{OC} exhibits a logarithmic increase with increasing light intensity, in agreement with the theoretical relationship described by equation (16). Since J_{SC} scales linearly with illumination, V_{OC} increases logarithmically. Physically, higher photon flux generates a larger population of photocarriers, leading to enhanced quasi-Fermi level splitting within the absorber and a corresponding rise in V_{OC} .

J_{SC} increases linearly with incident light intensity ($\frac{\partial(J_{SC})}{\partial(Intensity)} = \text{constant} = 187.52 \text{ mA/W}$), reflecting the direct proportionality between photon flux and the rate of photogenerated electron–hole pairs [75]. This proportionality indicates that photocarrier generation and collection remain efficient over the investigated intensity range, with no evidence of current saturation or transport-induced limitations.

A slight yet systematic increase in the FF is observed with increasing illumination intensity. This trend can be attributed to improved diode rectification and a reduced relative influence of resistive losses at higher photogenerated current densities, which together enhance the curvature of the J–V characteristics near the maximum power point.

Consequently, the PCE increases monotonically with illumination intensity, driven primarily by the linear enhancement of J_{SC} and the logarithmic rise in V_{OC} , with secondary contributions from FF improvement. Notably, the PCE remains substantial under low-intensity illumination and exhibits

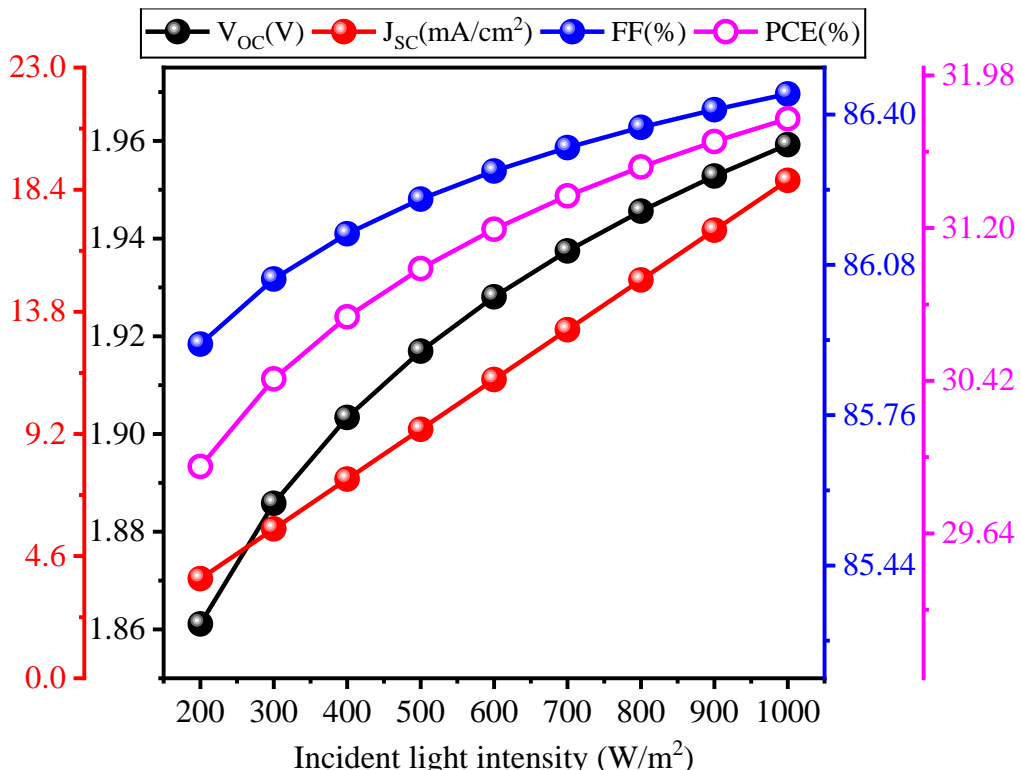


Fig. 18. Effect of incident light intensity on V_{OC} , J_{SC} , FF, and PCE of the device. The absorber, ETL and HTL thicknesses were fixed at 800 nm, 100 nm and 50 nm, respectively, while their doping densities were maintained at $3 \times 10^{17} \text{ cm}^{-3}$, $2 \times 10^{21} \text{ cm}^{-3}$ and 10^{20} cm^{-3} , respectively, which yielded the maximum PCE in section 3.4.3. All other material parameters were kept fixed at their default values (Tables 1-3).

stable behavior at higher irradiances, indicating the absence of recombination-induced rollover or resistive degradation across the investigated range.

3.5 Optimized Device

Based on the preceding optical and electrical analyses, the device parameters were systematically tuned to identify an optimized device configuration under standard operating conditions (AM1.5G illumination at 1000 W m^{-2} and 300 K). The optimized FTO/CeO₂/Cs₂AgBiBr₆/P3HT/Au device delivers a V_{OC} of 1.96 V, J_{SC} of 18.75 mA cm^{-2} , FF of 86.44%, and PCE of 31.76%. The corresponding J–V and P–V characteristics and external quantum efficiency (EQE) response are presented in Fig. 19.

To place these results in context, the optimized device performance was compared with recently reported Cs₂AgBiBr₆-based solar cells from both experimental and numerical studies published between 2022 and 2026 (Table 6). Experimentally reported efficiencies span a range from 0.19% to 6.37%, while simulation studies predicted efficiencies between 5.56% and 27.78%. The simulated optimal efficiency obtained in the present work exceeds the values reported in these studies, underscoring the potential of the proposed device architecture and the comprehensive 3D physics-based optimization strategy. It should be emphasized that the reported value represents the best-case simulated performance under idealized conditions.

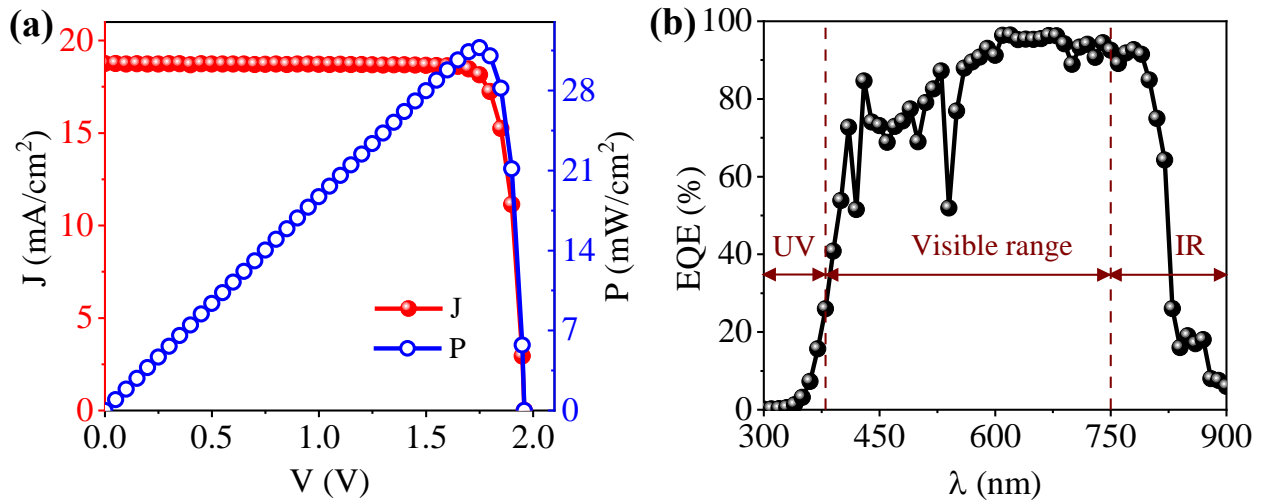


Fig. 19. (a) J–V and P (power)–V characteristics, and (b) EQE of the optimized FTO/CeO₂/Cs₂AgBiBr₆/P3HT/Au device. EQE was calculated using the formula [76]: $EQE(\lambda) = \frac{J(\lambda)}{q\Phi_{ph}(\lambda)}$, where J is the electron flux, in the form of electrical current (at short circuit) and Φ_{ph} is the incident photon flux. In panel (b), the AM1.5G spectrum is shown in the background in light brown, with values corresponding to normalized spectral irradiance. The UV (ultra-violet) region (300–380 nm), visible range (380–750 nm), and IR (infra-red) region (>750 nm) are indicated for reference. Thickness of different layers were set as: CeO₂ = 100 nm, Cs₂AgBiBr₆ = 800 nm, P3HT = 50 nm; doping densities were set as: CeO₂ = $2 \times 10^{21} \text{ cm}^{-3}$, Cs₂AgBiBr₆ = $3 \times 10^{17} \text{ cm}^{-3}$, P3HT = 10^{20} cm^{-3} . All other material parameters were kept fixed at their default values, as listed in (Tables 1–3).

Table 6. Comparison of photovoltaic performance of the proposed $\text{Cs}_2\text{AgBiBr}_6$ absorber-based solar cell with recent experimental and simulation studies (2022–2026).

Device structure	V_{OC} (V)	J_{SC} (mA/cm ²)	FF (%)	PCE (%)	Reference	Year
Experimental works						
FTO/SnO ₂ /Cs ₂ AgBiBr ₆ /Carbon	0.69	1.71	47.9	0.54	[77]	2023
FTO/TiO ₂ /Cs ₂ AgBiBr ₆ /Carbon	1.22	3.04	62.0	2.03	[78]	2023
ITO/SnO ₂ /Cs ₂ AgBiBr ₆ /Spiro-OMeTAD/Au	0.89	11.4	55.6	6.37	[28]	2022
SnO ₂ /Cs ₂ AgBiBr ₆ /Spiro-OMeTAD	0.92	11.4	60.93	6.37	[28]	2022
PTB7/Au/FTO/c-TiO ₂ /m-TiO ₂ /Cs ₂ AgBiBr ₆ /Spiro-OMeTAD/Ag	1.03	5.14	55.4	3.07	[79]	2022
FTO/c-TiO ₂ /Cs ₂ AgBiBr ₆ /Carbon	1.29	0.49	30.0	0.19	[80]	2022
FTO/c-TiO ₂ /m-TiO ₂ /Cs ₂ AgBiBr ₆ /Spiro-OMeTAD/Au	1.07	3.5	66.0	2.47	[81]	2022
TiO ₂ /Cs ₂ AgBiBr ₆ /Spiro-OMeTAD	1.08	3.55	64.0	2.46	[81]	2022
FTO/c-TiO ₂ /m-TiO ₂ /Cs ₂ AgBiBr ₆ /Carbon	1.2	2.61	71.0	2.22	[82]	2022
FTO/c-TiO ₂ /m-TiO ₂ /Cs ₂ AgBiBr ₆ /MoS ₂ /carbon	1.1	6.12	72.0	4.17	[83]	2022
FTO/c-TiO ₂ /m-TiO ₂ /Cs ₂ AgBiBr ₆ /poly[[4,8-bis(5-(2-ethylhexyl)-2-thienyl]benzo[1,2-b:4,5-b']]]	1.28	3.34	77.5	3.31	[84]	2022
FTO/c-TiO ₂ /m-TiO ₂ /Cs ₂ AgBiBr ₆ /Spiro-OMeTAD/Ag	1.05	1.77	71.7	1.33	[85]	2022
FTO/c-TiO ₂ /m-TiO ₂ /Cs ₂ AgBiBr ₆ /Spiro-OMeTAD/Ag	1.23	2.38	71.0	2.09	[86]	2022
FTO/c-TiO ₂ /m-TiO ₂ /D ₄₁₉ -Cs ₂ AgBiBr ₆ @Ti ₃ C ₂ Tx/Spiro-OMeTAD/Ag	0.72	8.85	70.1	4.47	[87]	2022
FTO/m-TiO ₂ /Cs ₂ AgBiBr ₆ /SnS QDs/carbon	1.02	3.74	51.0	1.95	[88]	2022
FTO/TiO ₂ /Cs ₂ Ag _{1-x} ZnxBiBr ₆ /Carbon	1.0	4.23	51.0	2.16	[89]	2022
ITO/SnO ₂ /Cs ₂ AgBiBr ₆ /P ₃ HT/MoO ₃ /PTAA/Au	1.06	2.8	65.0	1.94	[90]	2022
Simulation works						
FTO/TiO ₂ /Cs ₂ AgBiBr ₆ /Cu ₂ O/Au	1.71	23.33	76.24	27.78	[38]	2026
FTO/SnO ₂ /Cs ₂ AgBiBr ₆ /P ₃ HT/Al	1.79	13.26	75.41	17.56	[91]	2025
FTO/TiO ₂ /Cs ₂ AgBiBr ₆ /CuI/Au	1.04	8.54	62.37	5.56	[92]	2025
FTO/TiO ₂ /Cs ₂ AgBiBr ₆ /Cu ₂ O/Au	1.33	8.78	64.96	7.6	[92]	2025
FTO/TiO ₂ /Cs ₂ AgBiBr ₆ /CuSCN/Au	1.14	8.6	63.71	6.28	[92]	2025
FTO/TiO ₂ /Cs ₂ AgBiBr ₆ /GQDs/Au	0.814	24.55	76.69	15.33	[93]	2025
FTO/TiO ₂ /Cs ₂ AgBiBr ₆ /Spiro-OMEOTED/Au	1.06	8.55	62.53	5.68	[92]	2025
FTO/ZnO/Cs ₂ AgBiBr ₆ /CBTS/Au	1.42	19.978	89.958	25.562	[36]	2025
FTO/ZnO/Cs ₂ AgBiBr ₆ /CFTS/Au	1.13	22.08	62.93	15.65	[36]	2025
ITO/TiO ₂ /Cs ₂ AgBiBr ₆ /Cu ₂ O/Au	1.11	16.54	82.43	15.11	[94]	2025
FTO/WS ₂ /Cs ₂ AgBiBr ₆ /Spiro-OMeTAD/Au	1.5	18.86	85.02	24.16	[95]	2025

Device structure	V _{OC} (V)	J _{SC} (mA/cm ²)	FF (%)	PCE (%)	Reference	Year
FTO/TiO ₂ /IDL/Cs ₂ AgBiBr ₆ (gradient)/C	1.69	12.11	88.79	18.21	[96]	2025
FTO/AZnO/Cs ₂ AgBiBr ₆ /CNTS/Au	1.375	21.38	79.93	23.5	[48]	2024
FTO/CdZnS/Cs ₂ AgBiBr ₆ /CNTS/Au	1.372	21.41	78.82	23.15	[48]	2024
FTO/CdZnS/Cs ₂ AgBiBr ₆ /CNTS/Au	1.377	21.42	79.09	23.34	[97]	2024
FTO/LBSO/Cs ₂ AgBiBr ₆ /CNTS/Au	1.373	21.4	79.72	23.42	[48]	2024
FTO/Nb ₂ O ₅ /Cs ₂ AgBiBr ₆ /CNTS/Au	1.376	21.41	78.87	23.23	[48]	2024
FTO/SnO ₂ /Cs ₂ AgBiBr ₆ /CuI/Au	1.04	11.79	66.41	8.15	[98]	2024
FTO/ZnO/Cs ₂ AgBiBr ₆ /CNTS/Au	1.37	21.38	79.93	23.5	[48]	2024
FTO/AZO/Cs ₂ AgBiBr ₆ /ZnTe	1.5	21.35	83.87	26.89	[35]	2024
FTO/SnO ₂ /Cs ₂ AgBiBr ₆ /Spiro-OMeTAD/Cu	1.787	8.648	36.38	5.62	[99]	2024
FTO/WO ₃ /Cs ₂ AgBiBr ₆ /NiO/Cu-doped C	1.4	20.0	74.76	20.93	[100]	2024
FTO/C ₆₀ /Cs ₂ AgBiBr ₆ /MoS ₂ /Pt	0.84	32.28	85.77	23.49	[101]	2023
FTO/PCBM/Cs ₂ AgBiBr ₆ /NiOx/Au	2.49	8.17	76.16	15.49	[1]	2023
FTO/PCBM/Cs ₂ AgBiBr ₆ /NiOx/Au	2.49	11.49	77.03	21.92	[1]	2023
FTO/SnO ₂ /Cs ₂ AgBiBr ₆ /Spiro-OMeTAD/Au	1.3	17.44	62.59	14.29	[102]	2023
FTO/ZnO/Cs ₂ AgBiBr ₆ /Cu ₂ O/Au	0.86	16.56	53.84	7.66	[103]	2023
FTO/ZnO/Cs ₂ AgBiBr ₆ /NiO/Au	1.29	20.69	81.72	21.88	[103]	2023
ITO/CdS/Cs ₂ AgBiBr ₆ /CuAlO ₂ /Pt	1.642	4.913	88.74	7.16	[104]	2023
ITO/Spiro-OMeTAD/Cs ₂ AgBiBr ₆ /SnO ₂ /Au	1.278	23.3	88.21	26.3	[105]	2023
SnO ₂ /Cs ₂ AgBiBr ₆ /Me ₄ PAC	1.527	10.42	75.66	12.08	[106]	2023
Zn _{0.75} Mg _{0.25} O/Cs ₂ AgBiBr ₆ /Cu-doped NiO _x	1.68	14.81	80.54	20.06	[107]	2023
Zn _{0.75} Mg _{0.25} O/Cs ₂ AgBiBr ₆ /Cu ₂ O	1.39	14.8	77.47	16.07	[107]	2023
Zn _{0.75} Mg _{0.25} O/Cs ₂ AgBiBr ₆ /MASnBr ₃	1.66	14.81	80.42	19.86	[107]	2023
Zn _{0.75} Mg _{0.25} O/Cs ₂ AgBiBr ₆ /NiO _x	1.45	14.8	78.43	16.84	[107]	2023
Zn _{0.75} Mg _{0.25} O/Cs ₂ AgBiBr ₆ /P3HT	1.24	14.79	73.64	13.51	[107]	2023
Zn _{0.75} Mg _{0.25} O/Cs ₂ AgBiBr ₆ /Spiro-OMeTAD	1.44	14.8	78.0	16.72	[107]	2023
FTO/TiO ₂ /Cs ₂ AgBiBr ₆ /Spiro-OMeTAD/Au	0.9	11.09	66.61	6.68	[108]	2022
Ni/NiO _x /Cs ₂ AgBiBr ₆ /TiO ₂ /FTO/Al	1.33	21.46	88.53	25.38	[109]	2022
ZnO/Cs ₂ AgBiBr ₆ /NiO	1.29	20.69	81.72	21.88	[103]	2022
FTO/CeO ₂ / Cs ₂ AgBiBr ₆ /P3HT/Au	1.96	18.75	86.44	31.76	This work	2026

4. Conclusion

In this work, a physics-based three-dimensional numerical framework, grounded in Maxwell's electrodynamics and semiconductor drift-diffusion theory, was developed to investigate the performance-limiting factors and optimization pathways for $\text{Cs}_2\text{AgBiBr}_6$ -based lead-free double perovskite solar cells. A systematic screening of 25 ETL–HTL combinations, constructed from five representative electron transport layers (CeO_2 , AZO, C_{60} , PCBM, and WS_2) and five hole transport layers (P3HT, CuO, NiO, PEDOT:PSS, and MoO_3), identified the CeO_2 /P3HT pairing as the most promising architecture, delivering the highest power conversion efficiency among all evaluated configurations. Building on the FTO/ CeO_2 / $\text{Cs}_2\text{AgBiBr}_6$ /P3HT/Au stack, comprehensive optical and electrical analyses were conducted, covering optimization of layer thicknesses and doping densities, together with quantitative assessment of bulk and interfacial defect states, to resolve the coupled photogeneration, carrier transport, and recombination dynamics governing device operation. Optical analyses revealed strongly front-loaded photogeneration, with peak absorption localized near the ETL/absorber interface and generation rates on the order of $\sim 10^{20} \text{ cm}^{-3} \text{ s}^{-1}$ across the 400–800 nm spectral range. Importantly, generation profiles were calculated for each absorber, ETL, and HTL thickness variation, enabling realistic capture of optical redistribution and interference effects that are commonly neglected in typical device modeling. Systematic variation of absorber thickness and doping density demonstrated that V_{OC} and FF dominates efficiency gains at higher doping levels ($\geq 3 \times 10^{15} \text{ cm}^{-3}$), whereas photocurrent improvements associated with increased thickness are progressively offset by transport and recombination losses at excessive doping or thickness. Engineering of the CeO_2 layer revealed an optimal doping window ($> 10^{19} \text{ cm}^{-3}$) that enhances electron selectivity and device efficiency, while excessive ETL thickness ($> 0.5 \text{ } \mu\text{m}$) introduces parasitic absorption and transport resistance, reducing J_{SC} and PCE. Optimization of the P3HT layer exposed a pronounced non-monotonic dependencies of V_{OC} , FF, and PCE on both thickness and acceptor density, with higher efficiencies achieved at higher doping levels ($> 10^{19} \text{ cm}^{-3}$) and reduced thicknesses ($< 150 \text{ nm}$). Defect physics emerged as a dominant determinant of achievable performance. Bulk defect densities in $\text{Cs}_2\text{AgBiBr}_6$ exceeding $\sim 10^{14} \text{ cm}^{-3}$ drive a transition toward recombination-limited operation, sharply degrading photovoltaic metrics through reduced carrier lifetime and diffusion length. Interface defects exhibit asymmetric impact: the CeO_2 / $\text{Cs}_2\text{AgBiBr}_6$ interface shows relative tolerance to moderate trap densities ($\leq 10^9 \text{ cm}^{-2}$), whereas the P3HT/ $\text{Cs}_2\text{AgBiBr}_6$ interface demonstrates pronounced sensitivity, with continuous PCE degradation across the investigated defect range. Analysis of intrinsic recombination pathways revealed distinct threshold behavior. Device performance remains stable for radiative recombination coefficients below $\sim 10^{-11} \text{ cm}^3 \text{ s}^{-1}$ and Auger coefficients below $\sim 10^{-29} \text{ cm}^6 \text{ s}^{-1}$, beyond which rapid efficiency loss occurs due to severe carrier lifetime shortening and suppressed carrier collection. Thermal analyses indicate that device performance peaks near room temperature ($\sim 275 \text{ K}$), decreases afterwards and gradually saturates at higher temperatures, reflecting a dynamic balance between thermally induced carrier generation and recombination processes. Under varying illumination, the device exhibited linear J_{SC} scaling (187.52 mA/W) and logarithmic V_{OC} enhancement. PCE remains high across the examined range, showing no collapse at higher irradiances due to recombination or resistive effects, while maintaining substantial efficiency even under low-intensity conditions. By integrating optimized material, geometrical, and recombination parameters within physically realistic bounds, a peak simulated performance of $\text{V}_{\text{OC}} = 1.96 \text{ V}$, $\text{J}_{\text{SC}} = 18.75 \text{ mA cm}^{-2}$, FF = 86.44%, and PCE = 31.76% was achieved. These values represent theoretical performance projections under the current physically consistent modeling framework; practical devices may experience additional loss mechanisms—such as microstructural inhomogeneity, ion migration, and environmental degradation—that could moderate experimentally

achievable efficiencies. Overall, this study establishes a physically grounded device-engineering framework for $\text{Cs}_2\text{AgBiBr}_6$ solar cells, demonstrating how tightly coupled optical–electrical modeling can convert material-level characteristics into quantitatively guided device optimization strategies. The framework established here is broadly applicable to emerging lead-free perovskite systems and offers a scalable pathway toward experimentally realizable, high-efficiency photovoltaic technologies.

References

- [1] S. Beriha, A. Dikhit, and S. K. Tripathy, “Improving the efficiency of a FTO/PCBM/ $\text{Cs}_2\text{AgBiBr}_6$ /NiO_x/Au lead-free double perovskite solar cell using numerical simulation through optimizing the absorption layer thickness and work function of electrodes,” *Results Opt.*, vol. 12, p. 100467, Jul. 2023, doi: 10.1016/j.rio.2023.100467.
- [2] B. Roose *et al.*, “Local manufacturing of perovskite solar cells, a game-changer for low- and lower-middle income countries?,” *Energy Environ. Sci.*, vol. 15, no. 9, pp. 3571–3582, 2022, doi: 10.1039/D2EE01343F.
- [3] N. Kannan and D. Vakeesan, “Solar energy for future world: - A review,” *Renew. Sustain. Energy Rev.*, vol. 62, pp. 1092–1105, Sep. 2016, doi: 10.1016/j.rser.2016.05.022.
- [4] K. T. Arockiadoss, A.-D. Rasu Chettiar, M. F. Rahman, M. K. Hossain, and L. Marasamy, “Architecture guidelines for $\text{Cu}_2\text{Sr}_2\text{Sn}_4$ solar cells using chalcogenide and oxide hole transport layers by SCAPS-1D simulation,” *J. Phys. Chem. Solids*, vol. 203, p. 112732, Aug. 2025, doi: 10.1016/j.jpcs.2025.112732.
- [5] M. Aliaghayee, “Optimization of the Perovskite Solar Cell Design with Layer Thickness Engineering for Improving the Photovoltaic Response Using SCAPS-1D,” *J. Electron. Mater.*, vol. 52, no. 4, pp. 2475–2491, Apr. 2023, doi: 10.1007/s11664-022-10203-x.
- [6] P. Kung *et al.*, “A Review of Inorganic Hole Transport Materials for Perovskite Solar Cells,” *Adv. Mater. Interfaces*, vol. 5, no. 22, Nov. 2018, doi: 10.1002/admi.201800882.
- [7] A. Kojima, K. Teshima, Y. Shirai, and T. Miyasaka, “Organometal Halide Perovskites as Visible-Light Sensitizers for Photovoltaic Cells,” *J. Am. Chem. Soc.*, vol. 131, no. 17, pp. 6050–6051, May 2009, doi: 10.1021/ja809598r.
- [8] “Best Research-Cell Efficiencies, National Renewable Energy Laboratory [Online].” [Online]. Available: <https://www.nrel.gov/pv/cell-efficiency.html>
- [9] T. A. Chowdhury, M. A. Bin Zafar, M. Sajjad-Ul Islam, M. Shahinuzzaman, M. A. Islam, and M. U. Khandaker, “Stability of perovskite solar cells: issues and prospects,” *RSC Adv.*, vol. 13, no. 3, pp. 1787–1810, 2023, doi: 10.1039/D2RA05903G.
- [10] S. Ullah, T. Alshahrani, F. Khan, and F. Rasheed J., “Investigating the potential of lead-free $\text{Cs}_2\text{AgBiI}_6$ and $\text{Cs}_2\text{AgBiBr}_6$ double perovskites for photovoltaic applications,” *Mater. Today Commun.*, vol. 38, p. 108514, Mar. 2024, doi: 10.1016/j.mtcomm.2024.108514.
- [11] A. Al-Ahmed, M. Afzaal, F. Khan, and M. P. U. Haris, “Double-Perovskite Materials: Possibilities and Reality for a Better Solar Cell Device,” *IEEE J. Photovoltaics*, vol. 15, no. 3, pp. 380–392, 2025, doi: 10.1109/JPHOTOV.2025.3551499.
- [12] A. A. Hassan *et al.*, “Investigating the physical characteristics and photovoltaic performance of inorganic Ba_3NCI_3 perovskite utilizing DFT and SCAPS-1D simulations,” *Mater. Sci. Eng. B*, vol. 308, p. 117559, Oct. 2024, doi: 10.1016/j.mseb.2024.117559.
- [13] M. Pitaro, E. K. Tekelenburg, S. Shao, and M. A. Loi, “Tin Halide Perovskites: From Fundamental Properties to Solar Cells,” *Adv. Mater.*, vol. 34, no. 1, Jan. 2022, doi: 10.1002/adma.202105844.
- [14] M. Liu *et al.*, “B-Site Co-Alloying with Germanium Improves the Efficiency and Stability of All-Inorganic Tin-Based Perovskite Nanocrystal Solar Cells,” *Angew. Chemie Int. Ed.*, vol. 59, no. 49, pp. 22117–22125, Dec. 2020, doi: 10.1002/anie.2020008724.
- [15] S. W. Park, J. H. Heo, H. J. Lee, H. Kim, S. H. Im, and K.-H. Hong, “Compositional Design for High-Efficiency All-Inorganic Tin Halide Perovskite Solar Cells,” *ACS Energy Lett.*, vol. 8, no. 12, pp. 5061–5069, Dec. 2023, doi: 10.1021/acsenergylett.3c02032.
- [16] W. Ke and M. G. Kanatzidis, “Prospects for low-toxicity lead-free perovskite solar cells,” *Nat. Commun.*, vol.

10, no. 1, p. 965, Feb. 2019, doi: 10.1038/s41467-019-08918-3.

[17] I. López-Fernández *et al.*, “Lead-Free Halide Perovskite Materials and Optoelectronic Devices: Progress and Prospective,” *Adv. Funct. Mater.*, vol. 34, no. 6, Feb. 2024, doi: 10.1002/adfm.202307896.

[18] Y. Gao, Y. Pan, F. Zhou, G. Niu, and C. Yan, “Lead-free halide perovskites: a review of the structure–property relationship and applications in light emitting devices and radiation detectors,” *J. Mater. Chem. A*, vol. 9, no. 20, pp. 11931–11943, 2021, doi: 10.1039/D1TA01737C.

[19] S. H. Cho *et al.*, “Fabrication Strategies for 2D Halide Perovskite Towards Next-Generation Optoelectronic Applications,” *Int. J. Precis. Eng. Manuf. Technol.*, vol. 12, no. 1, pp. 349–380, Jan. 2025, doi: 10.1007/s40684-024-00663-3.

[20] W. Yu *et al.*, “Breaking the bottleneck of lead-free perovskite solar cells through dimensionality modulation,” *Chem. Soc. Rev.*, vol. 53, no. 4, pp. 1769–1788, 2024, doi: 10.1039/D3CS00728F.

[21] T. Song, Q.-X. Ma, Q. Wang, and H.-L. Zhang, “Design of two-dimensional halide perovskite composites for optoelectronic applications and beyond,” *Mater. Adv.*, vol. 3, no. 2, pp. 756–778, 2022, doi: 10.1039/D1MA00944C.

[22] J. Huang, H. Xiang, R. Ran, W. Zhou, W. Wang, and Z. Shao, “Fundamental understanding in the performance-limiting factors of Cs₂AgBiBr₆-based perovskite photovoltaics,” *Renew. Sustain. Energy Rev.*, vol. 191, p. 114187, Mar. 2024, doi: 10.1016/j.rser.2023.114187.

[23] T. Zhang, Z. Cai, and S. Chen, “Chemical Trends in the Thermodynamic Stability and Band Gaps of 980 Halide Double Perovskites: A High-Throughput First-Principles Study,” *ACS Appl. Mater. Interfaces*, vol. 12, no. 18, pp. 20680–20690, May 2020, doi: 10.1021/acsami.0c03622.

[24] P. Li, W. Gao, C. Ran, H. Dong, X. Hou, and Z. Wu, “Post-Treatment Engineering of Vacuum-Deposited Cs₂NaBiI₆ Double Perovskite Film for Enhanced Photovoltaic Performance,” *Phys. status solidi*, vol. 216, no. 23, Dec. 2019, doi: 10.1002/pssa.201900567.

[25] L. Zhang *et al.*, “Tuning Emission and Electron–Phonon Coupling in Lead-Free Halide Double Perovskite Cs₂AgBiCl₆ under Pressure,” *ACS Energy Lett.*, vol. 4, no. 12, pp. 2975–2982, Dec. 2019, doi: 10.1021/acsenergylett.9b02155.

[26] V. Murgulov *et al.*, “Double perovskite Cs₂AgBiBr₆ radiation sensor: synthesis and characterization of single crystals,” *J. Mater. Sci.*, vol. 57, no. 4, pp. 2758–2774, Jan. 2022, doi: 10.1007/s10853-021-06847-5.

[27] C. N. Savory, A. Walsh, and D. O. Scanlon, “Can Pb-Free Halide Double Perovskites Support High-Efficiency Solar Cells?,” *ACS Energy Lett.*, vol. 1, no. 5, pp. 949–955, Nov. 2016, doi: 10.1021/acsenergylett.6b00471.

[28] Z. Zhang *et al.*, “Hydrogenated Cs₂AgBiBr₆ for significantly improved efficiency of lead-free inorganic double perovskite solar cell,” *Nat. Commun.*, vol. 13, no. 1, p. 3397, Jun. 2022, doi: 10.1038/s41467-022-31016-w.

[29] A. H. Slavney, T. Hu, A. M. Lindenberg, and H. I. Karunadasa, “A Bismuth-Halide Double Perovskite with Long Carrier Recombination Lifetime for Photovoltaic Applications,” *J. Am. Chem. Soc.*, vol. 138, no. 7, pp. 2138–2141, 2016, doi: 10.1021/jacs.5b13294.

[30] G. Volonakis *et al.*, “Lead-Free Halide Double Perovskites via Heterovalent Substitution of Noble Metals,” *J. Phys. Chem. Lett.*, vol. 7, no. 7, pp. 1254–1259, Apr. 2016, doi: 10.1021/acs.jpclett.6b00376.

[31] M. Jakir Hossen *et al.*, “Recent progress on the efficiency and stability of lead-free Cs₂AgBiBr₆ double halide perovskite solar cells,” *Phys. Scr.*, vol. 100, no. 1, 2025, doi: 10.1088/1402-4896/ad9b59.

[32] E. Greul, M. L. Petrus, A. Binek, P. Docampo, and T. Bein, “Highly stable, phase pure Cs₂AgBiBr₆ double perovskite thin films for optoelectronic applications,” *J. Mater. Chem. A*, vol. 5, no. 37, pp. 19972–19981, 2017, doi: 10.1039/C7TA06816F.

[33] Y. Zou *et al.*, “Surface Reconstruction for Efficient Cs₂AgBiBr₆ Solar Cells,” *J. Phys. Chem. C*, vol. 127, no. 37, pp. 18301–18309, Sep. 2023, doi: 10.1021/acs.jpcc.3c04362.

[34] P. Fan *et al.*, “Single-Source Vapor-Deposited Cs₂AgBiBr₆ Thin Films for Lead-Free Perovskite Solar Cells,” *Nanomaterials*, vol. 9, no. 12, p. 1760, Dec. 2019, doi: 10.3390/nano9121760.

[35] S. Srivastava, R. Srivastava, D. Punetha, A. K. Sharma, and Y. K. Prajapati, “Enhancing the efficiency of lead-

free Cs₂AgBiBr₆ based double perovskite solar cells with optimizing ETLs and HTLs using SCAPS-1D,” *Chem. Phys. Lett.*, vol. 854, p. 141557, Nov. 2024, doi: 10.1016/j.cplett.2024.141557.

[36] E. Danladi, E. E. Oguzie, and F. I. Ezema, “Highly efficient 25.562% Cs₂AgBiBr₆ double perovskite solar cell with copper barium tin sulfide and ZnO as charge transport channels: an intuition from a theoretical study using SCAPS-1D,” *J. Photonics Energy*, vol. 15, no. 02, Mar. 2025, doi: 10.1117/1.JPE.15.024501.

[37] J. Hakami, “A comprehensive study to optimize organic/inorganic ETL and HTL materials on double perovskite layer Cs₂AgBiBr₆ solar cells with SCAPS 1D simulator,” *Results Eng.*, vol. 25, p. 104044, Mar. 2025, doi: 10.1016/j.rineng.2025.104044.

[38] M. Raj, A. Makhija, A. Kushwaha, and N. Goel, “Integrated First-Principles, SCAPS-1D, and ML Framework for Engineering CsAgBiBr₆ based Perovskite Solar Cell for IoT-Integrated Applications,” *Mater. Sci. Eng. B*, vol. 324, p. 119014, Feb. 2026, doi: 10.1016/j.mseb.2025.119014.

[39] A. Kowsar *et al.*, “An overview of solar cell simulation tools,” *Sol. Energy Adv.*, vol. 5, p. 100077, 2025, doi: 10.1016/j.seja.2024.100077.

[40] “COMSOL Multiphysics Reference Manual (Version 6.0).” www.comsol.com, pp. 1–2026. [Online]. Available: https://doc.comsol.com/6.0/doc/com.comsol.help.comsol/COMSOL_ReferenceManual.pdf

[41] K. G. Beepat, D. P. Sharma, A. Mahajan, D. Pathak, and V. Kumar, “Simulation of multijunction solar cell interfaces for enhancement of the power conversion efficiency,” *Discov. Appl. Sci.*, vol. 6, no. 6, p. 283, May 2024, doi: 10.1007/s42452-024-05930-1.

[42] J. Zhao *et al.*, “Simulation of Crystalline Silicon Photovoltaic Cells for Wearable Applications,” *IEEE Access*, vol. 9, pp. 20868–20877, 2021, doi: 10.1109/ACCESS.2021.3050431.

[43] J. Kim, S. Wong, G. Kim, Y.-B. Park, J. van Embden, and E. Della Gaspera, “Transparent electrodes based on spray coated fluorine-doped tin oxide with enhanced optical, electrical and mechanical properties,” *J. Mater. Chem. C*, vol. 8, no. 41, pp. 14531–14539, 2020, doi: 10.1039/D0TC03314F.

[44] P.-H. Lee *et al.*, “Work-Function-Tunable Electron Transport Layer of Molecule-Capped Metal Oxide for a High-Efficiency and Stable p–i–n Perovskite Solar Cell,” *ACS Appl. Mater. Interfaces*, vol. 12, no. 41, pp. 45936–45949, Oct. 2020, doi: 10.1021/acsami.0c10717.

[45] T. Kim, J. Lim, and S. Song, “Recent Progress and Challenges of Electron Transport Layers in Organic–Inorganic Perovskite Solar Cells,” *Energies*, vol. 13, no. 21, p. 5572, Oct. 2020, doi: 10.3390/en13215572.

[46] M. Ferdous Rahman, M. Al Ijajul Islam, M. Chowdhury, L. Ben Farhat, S. Ezzine, and A. T. M. Saiful Islam, “Efficiency improvement of CsSnI₃ based heterojunction solar cells with P3HT HTL: A numerical simulation approach,” *Mater. Sci. Eng. B*, vol. 307, p. 117524, Sep. 2024, doi: 10.1016/j.mseb.2024.117524.

[47] R. S. Singh, R. D. Patidar, K. Deshmukh, A. Gautam, and A. Kumar, “Influence of CuO Layer on the Performance of Thin-Film Copper Indium Gallium Selenide Solar Cells: A Numerical Analysis,” *J. Electron. Mater.*, vol. 54, no. 1, pp. 609–619, Jan. 2025, doi: 10.1007/s11664-024-11588-7.

[48] M. S. Uddin *et al.*, “An In-Depth Investigation of the Combined Optoelectronic and Photovoltaic Properties of Lead-Free Cs₂AgBiBr₆ Double Perovskite Solar Cells Using DFT and SCAPS-1D Frameworks,” *Adv. Electron. Mater.*, vol. 10, no. 5, May 2024, doi: 10.1002/aelm.202300751.

[49] P. Zhou *et al.*, “Efficient and stable mixed perovskite solar cells using P3HT as a hole transporting layer,” *J. Mater. Chem. C*, vol. 6, no. 21, pp. 5733–5737, 2018, doi: 10.1039/C8TC01345D.

[50] M. K. Hossain *et al.*, “An extensive study on multiple ETL and HTL layers to design and simulation of high-performance lead-free CsSnCl₃-based perovskite solar cells,” *Sci. Rep.*, vol. 13, no. 1, p. 2521, Feb. 2023, doi: 10.1038/s41598-023-28506-2.

[51] M. K. Hossain, M. H. K. Rubel, G. F. I. Toki, I. Alam, M. F. Rahman, and H. Bencherif, “Effect of Various Electron and Hole Transport Layers on the Performance of CsPbI₃-Based Perovskite Solar Cells: A Numerical Investigation in DFT, SCAPS-1D, and wxAMPS Frameworks,” *ACS Omega*, vol. 7, no. 47, pp. 43210–43230, Nov. 2022, doi: 10.1021/acsomega.2c05912.

[52] H. Alipour and A. Ghadimi, “Optimization of lead-free perovskite solar cells in normal-structure with $\text{altimg}="si1.svg"$ $\langle mrow \rangle$ $\langle msup \rangle$ $\langle mtext \rangle$ WO $\langle /mtext \rangle$ $\langle mn \rangle$ 3 $\langle /mn \rangle$ $\langle msup \rangle$ $\langle /mrow \rangle$ $\langle /math \rangle$ and water-

free PEDOT: PSS composite for hole transport layer by SCAPS-1D simulation," *Opt. Mater. (Amst.)*, vol. 120, p. 111432, Oct. 2021, doi: 10.1016/j.optmat.2021.111432.

[53] Zulfanizam Abdul Wahab *et al.*, "Insights of MoO₃ HTL in Perovskite Solar Cells from a Simulation Perspective," *Int. J. Nanoelectron. Mater.*, vol. 17, no. December, pp. 31–38, Dec. 2024, doi: 10.58915/ijneam.v17iDecember.1604.

[54] H. El-assib *et al.*, "High-performance optimization and analysis of Cs₂CuSbCl₆-Based lead-free double perovskite solar cells with theoretical efficiency exceeding 27 %," *Renew. Energy*, vol. 239, p. 122092, Feb. 2025, doi: 10.1016/j.renene.2024.122092.

[55] Y. Gan *et al.*, "Numerical Investigation Energy Conversion Performance of Tin-Based Perovskite Solar Cells Using Cell Capacitance Simulator," *Energies*, vol. 13, no. 22, p. 5907, Nov. 2020, doi: 10.3390/en13225907.

[56] Naureen, Sadanand, S. Rai, R. K. Yadav, P. Lohia, and D. K. Dwivedi, "A simulation study of quantum dot solar cells using two distinct ETL of WO₃ and WS₂," *Opt. Quantum Electron.*, vol. 55, no. 6, p. 541, Jun. 2023, doi: 10.1007/s11082-023-04809-6.

[57] S. Ben Ameur *et al.*, "Physical investigations on undoped and Fluorine doped SnO₂ nanofilms on flexible substrate along with wettability and photocatalytic activity tests," *Mater. Sci. Semicond. Process.*, vol. 61, pp. 17–26, Apr. 2017, doi: 10.1016/j.mssp.2016.12.019.

[58] H. J. Mohamad, Y. M. Abdul-Husaain, and U. A. S. Al-Jarah, "The structural, optical, and morphological properties of NiO-Cu prepared by spray pyrolysis technique," *Microw. Opt. Technol. Lett.*, vol. 62, no. 11, pp. 3519–3526, Nov. 2020, doi: 10.1002/mop.32500.

[59] "Refractive Index Database: PEDOT:PSS." [Online]. Available: <https://refractiveindex.info/?shelf=other&book=PEDOT-PSS&page=Chen>

[60] Q. H. Li, D. Zhu, W. Liu, Y. Liu, and X. C. Ma, "Optical properties of Al-doped ZnO thin films by ellipsometry," *Appl. Surf. Sci.*, vol. 254, no. 10, pp. 2922–2926, Mar. 2008, doi: 10.1016/j.apsusc.2007.09.104.

[61] M. Ullah, A. M. Rana, U. Mehtab, and M. Farooq, "Study of structural, electronic and optical properties of co-doped CeO₂ using the density functional theory (DFT) method," *Mater. Sci. Semicond. Process.*, vol. 130, p. 105800, Aug. 2021, doi: 10.1016/j.mssp.2021.105800.

[62] F. Gami, I. Guizani, M. A. Sebak, A. A. Abuelwafa, and M. M. Mostafa, "Investigation of structural, optical and electrical properties of PCBM/ZnOEP thin films," *Opt. Mater. (Amst.)*, vol. 134, p. 113093, Dec. 2022, doi: 10.1016/j.optmat.2022.113093.

[63] "Refractive Index Database: WS₂." [Online]. Available: <https://refractiveindex.info/?shelf=main&book=WS2&page=Jung>

[64] D. Datta and S. Kumar, "Growth and ellipsometric studies on C₆₀ thin films for solar cell applications," *J. Appl. Phys.*, vol. 106, no. 7, Oct. 2009, doi: 10.1063/1.3239853.

[65] L. Hrostea, M. Girtan, R. Mallet, and L. Leontie, "Optical and Morphological Properties of P3HT and P3HT: PCBM Thin Films Used in Photovoltaic Applications," *IOP Conf. Ser. Mater. Sci. Eng.*, vol. 374, p. 012015, Jun. 2018, doi: 10.1088/1757-899X/374/1/012015.

[66] M. Nesa, M. A. Momin, M. Sharmin, and A. H. Bhuiyan, "Structural, optical and electronic properties of CuO and Zn doped CuO: DFT based First-principles calculations," *Chem. Phys.*, vol. 528, p. 110536, Jan. 2020, doi: 10.1016/j.chemphys.2019.110536.

[67] "Refractive Index Database: MoO₃." [Online]. Available: <https://refractiveindex.info/?shelf=main&book=MoO3&page=Stelling>

[68] C. Multiphysics, "Introduction To Wave Optics Module." [Online]. Available: <https://doc.comsol.com/6.0/doc/com.comsol.help.woptics/IntroductionToWaveOpticsModule.pdf>

[69] A. A. Zaky, S. Elewa, S. Alyahya, M. Al-Dhaifallah, H. Rezk, and B. Yousif, "Mitigation of Temperature Effects and Performance Enhancement of Perovskite Solar Cells Using Nano-Pyramids Grating," *IEEE Access*, vol. 11, no. April, pp. 36399–36408, 2023, doi: 10.1109/ACCESS.2023.3266240.

[70] M. T. Bin Kashem and S. A. Esha, "Advancing lead-free all-inorganic NaSnCl₃ based perovskite solar cell for high efficiency: Computational optimization of charge transport layers and material parameters," *Mater. Today*

Commun., vol. 47, p. 113192, Jul. 2025, doi: 10.1016/j.mtcomm.2025.113192.

- [71] J. Chen *et al.*, “Improving the performance of lead-free Cs₂AgBiBr₆ double perovskite solar cells by passivating Br vacancies,” *J. Mater. Chem. C*, vol. 12, no. 35, pp. 14074–14084, 2024, doi: 10.1039/D4TC02339K.
- [72] D. Liu, C. M. Perez, A. S. Vasenko, and O. V. Prezhdo, “Ag–Bi Charge Redistribution Creates Deep Traps in Defective Cs₂AgBiBr₆: Machine Learning Analysis of Density Functional Theory,” *J. Phys. Chem. Lett.*, vol. 13, no. 16, pp. 3645–3651, Apr. 2022, doi: 10.1021/acs.jpclett.2c00869.
- [73] A. Alghafis and M. K. S. Bin Rafiq, “Impact of interface defects and doping levels on bismuth-based double perovskite solar cells: a numerical modeling approach,” *Opt. Quantum Electron.*, vol. 57, no. 4, p. 245, Apr. 2025, doi: 10.1007/s11082-025-08158-4.
- [74] P. Singh and N. M. Ravindra, “Temperature dependence of solar cell performance - An analysis,” *Sol. Energy Mater. Sol. Cells*, vol. 101, no. October, pp. 36–45, 2012, doi: 10.1016/j.solmat.2012.02.019.
- [75] J. H. Kim, K. J. Moon, J. M. Kim, D. Lee, and S. H. Kim, “Effects of various light-intensity and temperature environments on the photovoltaic performance of dye-sensitized solar cells,” *Sol. Energy*, vol. 113, pp. 251–257, Mar. 2015, doi: 10.1016/j.solener.2015.01.012.
- [76] J. Bisquert, *The physics of solar cells: Perovskites, organics, and photovoltaic fundamentals*. 2017. doi: 10.1201/b22380.
- [77] S. Liu, H. Zhang, Y. Xing, Q. He, S. Han, and H. Zhu, “Thermodynamically regulated preparation of high performance for carbon-based Cs₂AgBiBr₆ perovskite solar cells,” *Mater. Sci. Semicond. Process.*, vol. 154, p. 107193, Feb. 2023, doi: 10.1016/j.mssp.2022.107193.
- [78] J. Duan *et al.*, “MACl enhanced electron extraction in all-inorganic Cs₂AgBiBr₆ perovskite photovoltaics,” *Chem. Commun.*, vol. 59, no. 9, pp. 1173–1176, 2023, doi: 10.1039/D2CC06432D.
- [79] X. Yang *et al.*, “Thiourea with sulfur-donor as an effective additive for enhanced performance of lead-free double perovskite photovoltaic cells,” *J. Colloid Interface Sci.*, vol. 628, pp. 476–485, Dec. 2022, doi: 10.1016/j.jcis.2022.07.165.
- [80] F. Schmitz *et al.*, “High Open-Circuit Voltage Cs₂AgBiBr₆ Carbon-Based Perovskite Solar Cells via Green Processing of Ultrasonic Spray-Coated Carbon Electrodes from Waste Tire Sources,” *ChemSusChem*, vol. 15, no. 22, Nov. 2022, doi: 10.1002/cssc.202201590.
- [81] M. T. Sirtl *et al.*, “2D/3D Hybrid Cs₂AgBiBr₆ Double Perovskite Solar Cells: Improved Energy Level Alignment for Higher Contact-Selectivity and Large Open Circuit Voltage,” *Adv. Energy Mater.*, vol. 12, no. 7, Feb. 2022, doi: 10.1002/aenm.202103215.
- [82] J. Li *et al.*, “Pinning Bromide Ion with Ionic Liquid in Lead-Free Cs₂AgBiBr₆ Double Perovskite Solar Cells,” *Adv. Funct. Mater.*, vol. 32, no. 25, Jun. 2022, doi: 10.1002/adfm.202112991.
- [83] B. Pang *et al.*, “Improved charge extraction and atmospheric stability of all-inorganic Cs₂AgBiBr₆ perovskite solar cells by MoS₂ nanoflakes,” *Sol. Energy Mater. Sol. Cells*, vol. 246, p. 111932, Oct. 2022, doi: 10.1016/j.solmat.2022.111932.
- [84] B. Li *et al.*, “Efficient and stable Cs₂AgBiBr₆ double perovskite solar cells through in-situ surface modulation,” *Chem. Eng. J.*, vol. 446, p. 137144, Oct. 2022, doi: 10.1016/j.cej.2022.137144.
- [85] D. Zhao *et al.*, “Overcoming the Limitation of Cs₂AgBiBr₆ Double Perovskite Solar Cells Through Using Mesoporous TiO₂ Electron Extraction Layer,” *ENERGY Environ. Mater.*, vol. 5, no. 4, pp. 1317–1322, Oct. 2022, doi: 10.1002/eem2.12249.
- [86] A. Yang *et al.*, “VOC over 1.2 V for Cs₂AgBiBr₆ solar cells based on formamidinium acetate additive,” *J. Mater. Sci. Mater. Electron.*, vol. 33, no. 23, pp. 18758–18767, Aug. 2022, doi: 10.1007/s10854-022-08724-6.
- [87] L. Yang *et al.*, “Performance improvement of dye-sensitized double perovskite solar cells by adding Ti₃C₂T MXene,” *Chem. Eng. J.*, vol. 446, p. 136963, Oct. 2022, doi: 10.1016/j.cej.2022.136963.
- [88] Y. Ou *et al.*, “Efficiency improvement of Cs₂AgBiBr₆ perovskite solar cells with modification of SnS quantum dots,” *Mater. Lett.*, vol. 312, p. 131672, Apr. 2022, doi: 10.1016/j.matlet.2022.131672.

[89] Y. Ou *et al.*, “Boosting the stability and efficiency of Cs₂AgBiBr₆ perovskite solar cells via Zn doping,” *Opt. Mater. (Amst.)*, vol. 129, p. 112452, Jul. 2022, doi: 10.1016/j.optmat.2022.112452.

[90] Z. Zhang *et al.*, “Efficient Nonlead Double Perovskite Solar Cell with Multiple Hole Transport Layers,” *ACS Appl. Energy Mater.*, vol. 3, no. 10, pp. 9594–9599, Oct. 2020, doi: 10.1021/acsaem.0c01066.

[91] M. Z. Arif *et al.*, “Comprehensive Analysis of Cesium Silver Bismuth Bromide Perovskite Solar Cells: Enhancing Performance through Optimization and Modeling,” *Phys. status solidi*, vol. 222, no. 16, Aug. 2025, doi: 10.1002/pssa.202500159.

[92] A. Raj, M. Kumar, D. V. Singh, B. Singh, D. K. Dwivedi, and A. Anshul, “Physical parameter optimization and band alignment approach for efficiency improvement in Cs₂AgBiBr₆ based lead-free perovskite solar cells,” *Sci. Rep.*, vol. 15, no. 1, p. 32868, Sep. 2025, doi: 10.1038/s41598-025-02203-8.

[93] M. A. Saifee, M. Ali, F. F. A. Khan, A. K. Srivastava, J. Ali, and M. S. Khan, “Design and performance optimization of a lead-free Cs₂AgBiBr₆ perovskite solar cell with graphene quantum dot hole transport layer using SCAPS-1D and machine learning,” *J. Opt.*, Feb. 2025, doi: 10.1007/s12596-025-02539-4.

[94] M. Mehrabian, M. Taleb-Abbas, and O. Akhavan, “Comparing the performances of Cs₂TiBr₆, Cs₂AgBiBr₆, and Cs₂PtI₆ halide compositions in double perovskite photovoltaic devices,” *Mater. Renew. Sustain. Energy*, vol. 14, no. 2, p. 38, Aug. 2025, doi: 10.1007/s40243-025-00311-z.

[95] M. A. Hachimi *et al.*, “Combined experimental and numerical approach for the optimization of double Cs₂AgBiBr₆ perovskite solar cells: Ab initio study, simulation and performance comparison,” *Solid State Sci.*, vol. 169, p. 108101, Nov. 2025, doi: 10.1016/j.solidstatesciences.2025.108101.

[96] W. Yang, W. Li, Q. Liu, and Y. Jin, “Design and simulation of gradient-structured Cs₂AgBiBr₆ carbon-based double perovskite solar cell for boosting photovoltaic performance,” *Sol. Energy*, vol. 290, p. 113347, Apr. 2025, doi: 10.1016/j.solener.2025.113347.

[97] S. Rawat, J. Madan, and A. Verma, “Investigating the Efficiency of Photovoltaic Cells Using Cs₂AgBiBr₆ Perovskite: Analyzing the Impact of Absorber Layer Thickness,” in *2024 Second International Conference on Microwave, Antenna and Communication (MAC)*, IEEE, Oct. 2024, pp. 1–4, doi: 10.1109/MAC61551.2024.10837548.

[98] M. Z. Arif, M. Rahman, N. K. Chowdhury, S. Islam, M. Z. Alam, and M. S. Reza, “Numerical investigation and design optimization for enhanced efficiency of Cs₂AgBiBr₆ perovskite solar cell,” *Phys. Scr.*, vol. 99, no. 10, p. 105110, Oct. 2024, doi: 10.1088/1402-4896/ad7545.

[99] S. Das *et al.*, “Electron Transport Layer Material Optimization for Cs₂AgBiBr₆ Based Solar Cell Using SCAPS,” *J. Nano- Electron. Phys.*, vol. 16, no. 1, pp. 01014-1-01014-4, 2024, doi: 10.21272/jnep.16(1).01014.

[100] A. S. M. Mosabbir *et al.*, “Optimizing lead-free Cs₂AgBiBr₆ double perovskite solar cells: insights from SCAPS and FDTD simulations,” *Sustain. Energy Fuels*, vol. 8, no. 18, pp. 4311–4323, 2024, doi: 10.1039/D4SE00958D.

[101] N. Jaiswal, D. Kumari, R. Shukla, and S. K. Pandey, “Design and Performance Optimization of Eco-friendly Cs₂AgBiBr₆ Double Perovskite Solar Cell,” *J. Electron. Mater.*, vol. 52, no. 12, pp. 7842–7849, Dec. 2023, doi: 10.1007/s11664-023-10705-2.

[102] T. I. Alanazi, “Design and Device Numerical Analysis of Lead-Free Cs₂AgBiBr₆ Double Perovskite Solar Cell,” *Crystals*, vol. 13, no. 2, p. 267, Feb. 2023, doi: 10.3390/crust13020267.

[103] H. I. Alkhammash, M. Mottakin, M. M. Hossen, M. Akhtaruzzaman, and M. J. Rashid, “Design and defect study of Cs₂AgBiBr₆ double perovskite solar cell using suitable charge transport layers,” *Semicond. Sci. Technol.*, vol. 38, no. 1, p. 015005, Jan. 2023, doi: 10.1088/1361-6641/aca42b.

[104] I. Chabri, Y. Benhouria, A. Oubelkacem, A. Kaiba, I. Essaoudi, and A. Ainane, “Cs₂AgBiBr₆-based perovskite solar cell: A novel combination of ITO/CdS/ Cs₂AgBiBr₆/CuAlO₂/Pt, with inorganic charge transport layers,” *Optik (Stuttg.)*, vol. 274, p. 170560, Mar. 2023, doi: 10.1016/j.ijleo.2023.170560.

[105] H. Sabbah, Z. Abdel Baki, R. Mezher, and J. Arayro, “SCAPS-1D Modeling of Hydrogenated Lead-Free Cs₂AgBiBr₆ Double Perovskite Solar Cells with a Remarkable Efficiency of 26.3%,” *Nanomaterials*, vol. 14, no. 1, p. 48, Dec. 2023, doi: 10.3390/nano14010048.

- [106] N. Shrivastav *et al.*, “Optimizing the performance of Cs₂AgBiBr₆ based solar cell through modification of electron and hole transport layers,” *Mater. Today Commun.*, vol. 36, p. 106761, Aug. 2023, doi: 10.1016/j.mtcomm.2023.106761.
- [107] P. Kumar and A. Kumar, “High-performance optimization and analysis of Cs₂AgBiBr₆-based lead-free double perovskite solar cells,” *J. Mater. Sci. Mater. Electron.*, vol. 34, no. 26, p. 1810, Sep. 2023, doi: 10.1007/s10854-023-11225-9.
- [108] A. Raj, M. Kumar, A. Kumar, A. Laref, and A. Anshul, “Investigating the potential of lead-free double perovskite $\text{Cs}_2\text{AgBiBr}_6$ material for solar cell applications: A theoretical study,” *Int. J. Energy Res.*, vol. 46, no. 10, pp. 13801–13819, Aug. 2022, doi: 10.1002/er.8099.
- [109] M. R. Iftekhar, M. G. Rabbani, A. Hosen, M. S. Islam, M. S. Mian, and S. R. Al Ahmed, “Simulating the electrical characteristics of a highly efficient Cs₂AgBiBr₆-based perovskite solar cell with NiO x hole transport layer,” in *2022 International Conference on Advancement in Electrical and Electronic Engineering (ICAEEE)*, IEEE, Feb. 2022, pp. 1–4. doi: 10.1109/ICAEEE54957.2022.9836484.